Macrophages orchestrate the expansion of a pro-angiogenic perivascular niche during cancer progression

James W. Opzoomer[1,2], Joanne E. Anstee[1], Isaac Dean[3], Emily J. Hill[1], Ihssane Bouybayoune[1], Jonathan Caron[1], Tamara Muliaditan[1,4], Peter Gordon[1], Dominika Sosnowska[1], Rosamond Nuamah[5], Sarah E. Pinder[1], Tony Ng[1,6], Francesco Dazzi[1], Shahram Kordasti[7], David R. Withers[3], Toby Lawrence[8,9,10] and James N. Arnold[1]

[1]School of Cancer and Pharmaceutical Sciences, King's College London, London, SE1 1UL, United Kingdom.
[2]Current address: UCL Cancer Institute, University College London, London, WC1E 6DD, United Kingdom.
[3]Institute of Immunology and Immunotherapy, College of Medical and Dental Sciences, University of Birmingham, B15 2TT, United Kingdom.
[4]Current address: Department of Pharmaceutical Sciences, Faculty of Science, Utrecht University, Utrecht, Netherlands.
[5]NIHR BRC Genomics Facility, Guy's and St Thomas' NHS Foundation Trust, King's College London, Guy's Hospital, SE1 9RT, United Kingdom.
[6]UCL Cancer Institute, University College London, London, WC1E 6DD, United Kingdom.
[7]Department of Haematological Medicine, School of Cancer and Pharmaceutical Sciences, King's College London, Denmark Hill, London, SE5 9NU, United Kingdom.
[8]Centre for Inflammation Biology and Cancer Immunology, School of Immunology & Microbial Sciences, King's College London, London, SE1 1UL, United Kingdom.
[9]Aix Marseille University, CNRS, INSERM, CIML, Marseille, France.
[10]Henan Key Laboratory of Immunology and Targeted Therapy, School of Laboratory Medicine, Xinxiang Medical University, Xinxiang, China.

Short title

Macrophages and the perivascular niche in cancer

Teaser

Perivascular macrophages orchestrate the expansion of pericyte-like mesenchymal cells to create a pro-angiogenic niche in cancer.

Keywords

Tumor, stroma, perivascular, macrophage, mesenchymal, fibroblast, pericyte, niche

Abstract

Tumor associated macrophages (TAMs) are a highly plastic stromal cell type which support cancer progression. Using single-cell RNA-sequencing of TAMs from a spontaneous murine model of mammary adenocarcinoma (*MMTV-PyMT*) we characterize a subset of these cells expressing lymphatic vessel endothelial hyaluronic acid receptor 1 (Lyve-1) which spatially reside proximal to blood vasculature. We demonstrate that Lyve-1$^+$ TAMs support tumor growth and identify a pivotal role for these cells in maintaining a population of perivascular mesenchymal cells which express alpha-smooth muscle actin and phenotypically resemble pericytes. Using photolabeling techniques we show that mesenchymal cells maintain their prevalence in the growing tumor through proliferation and uncover a role for Lyve-1$^+$ TAMs in orchestrating a selective platelet-derived growth factor-CC-dependent expansion of the perivascular mesenchymal population, creating a pro-angiogenic niche. This study highlights the inter-reliance of the immune and non-immune stromal network which support cancer progression and provides therapeutic opportunities for tackling the disease.

Introduction

The stroma in cancer is composed of a variety of non-malignant immune and mesenchymal cell populations which facilitate tumor progression (*1*). Although a variety of pro-tumoral processes have been characterized for the individual cell populations which compose the stroma, it is apparent that these cells are not functioning autonomously but in concert with one another as part of a wider network of cross-communication to facilitate disease progression (*2*). Identifying non-redundant signaling pathways within the stromal network is desirable, as therapeutically targeting these signals could result in an unraveling of the stromal support network upon which the malignant tumor cells rely.

Macrophages form a major part of the stromal cell infiltrate in solid tumors (*3*), and are highly plastic to their environment which creates phenotypic and functional diversity within the population (*1, 4-10*). Tumors exploit the plastic nature of macrophages, which we collectively refer to as tumor-associated macrophages 'TAMs', to facilitate disease progression through promoting angiogenesis (*11, 12*), immune suppression (*1, 13*), chemotherapeutic resistance

(*14-16*) and tumor cell migration and metastasis (*4, 17-21*). Although the pro-tumoral function of TAMs is well described, less is known about their 'cellular' networks and the niches they support. This study highlights the inter-reliance of the immune-mesenchymal stromal network in cancer. Unlike immune cells which are readily recruited into the tumor microenvironment from the systemic circulation (*19, 22*), we demonstrate that mesenchymal stromal populations rely on local proliferation to expand with tumor growth. Using the spontaneous *MMTV-PyMT* murine model of breast cancer, we characterize a sub-population of TAMs which are defined by their selective expression of lymphatic vessel endothelial hyaluronic acid receptor 1 (Lyve-1) and spatial proximity to blood vasculature. We demonstrate that perivascular Lyve-1+ TAMs play a fundamental role in orchestrating the expansion of a population of pericyte-like mesenchymal cells which create a pro-angiogenic perivascular niche. This study highlights a role for perivascular TAMs in shaping the heterogeneity of the mesenchymal cell population in cancer and implicates their expression of platelet derived growth factor-CC (PDGF-CC) as a therapeutic target in the process.

Results and Discussion

To resolve the phenotypic heterogeneity of TAMs within the tumor microenvironment, CD45+Ly6G-CD11b+F4/80hi cells, which represented a broad gating strategy to encompass all TAMs, were FACs cell-sorted from enzyme-dispersed tumors from *MMTV-PyMT* mice (*23*) (fig. S1A). The TAMs were then subjected to the droplet-based 10X Genomics Platform for single cell RNA-sequencing (scRNA-seq; Fig. 1A). A total of 9,039 TAMs were sequenced across three individual tumors. Unsupervised graph-based clustering of the transcriptomes, visualized using *UMAP* (*24*), revealed eight distinct transcriptomic TAM clusters (Fig. 1B-D and fig. S1B,C). The presence of these transcriptomic clusters, despite the tumors being spontaneous, were conserved across the three tumors analyzed (Fig. 1E). Gene Ontology (GO) analysis of the transcriptional programs within these clusters revealed diversity in both the number and type of biological pathways that were active. One cluster (TAM08) represented a highly proliferative TAM state, indicating that TAMs are capable of proliferation in the tumor microenvironment, however the transcriptome of this TAM subset was dominated singularly by cell-cycle associated genes and so was not carried forward for further functional analysis (Fig. 1F and fig. S1D). Interestingly, the TAM clusters with few enriched GO terms, that appeared to be the least polarized in their gene expression profile (TAM01 and 02), represented almost a quarter of TAMs within the tumor (23.3% ± 3.4 of all TAMs analyzed), suggesting that a significant proportion of TAMs remain relatively unspecialized in their role (Fig. 1E,F and fig. S1E). Trajectory inference analysis using

Slingshot (*25*) and diffusion maps was used to align the 7 identified clusters by transcriptomic similarity into a polarization model with three clusters, TAM04, 06 and 07 predicted as possible polarization extremes compared to the relatively unspecialized TAM01, between which all *MMTV-PyMT* TAM transcriptomes fall between (Fig. 1G,H and fig. S2). The three clusters representing possible polarization extremes were analyzed for their enrichment of M1/M2 (*26*) programs using the marker gene list of Orecchioni *et al* (*27*). This analysis highlighted TAM04 to be skewed towards an inflammatory (M1-like) transcriptome (Fig. 2A,B) which were more enriched for expression of inflammatory genes representative of a cellular response to type-1 interferons such as *Irf7* and *Isg15.* TAM06 and TAM07 possessed a more pro-tumoral (M2-like) transcriptome (Fig. 2A,B). TAM06 was more enriched for anti-inflammatory genes such as *Il10,* whereas both TAM06 and TAM07 were enriched in *Ccl2*, *Mmp19*, *Hb-egf* and also *Mrc1* (the gene for MRC1/CD206) (*28*). However, TAM06 and TAM07 were functionally distinct in many of their enriched GO biological pathways, with a preferential skewing of TAM06 towards angiogenic processes and TAM07 towards immune regulation, highlighting a specialized sub-division of roles within the tumor (Fig. 2C,D). Flow cytometry analysis of gated F4/80^{hi} TAMs stained for markers identified within the scRNA-seq analysis, confirmed that similar TAM sub-populations could be distinguished using the predicted protein markers in *MMTV-PyMT* tumors. TAM06 and TAM07 subsets predicted by the scRNA-seq analysis could be differentiated based on their expression level of CD206, MHCII, and the lymphatic vessel endothelial hyaluronic acid receptor 1 (Lyve-1) (Fig. 2E,F), into the predicted polarization extremes of CD206^{hi}MHCII^{lo}Lyve-1^{+} (Lyve-1^{+} TAMs; TAM06) and CD206^{int}MHCII^{hi}Lyve-1^{-} (TAM07). The Lyve-1^{+} TAM subset accounted for 10.7±3.5% of total TAMs and 1.4±0.4% of live cells within the tumor (Fig. 2F). To validate that the populations identified in the scRNA-seq and flow cytometry data were equivalent, the FACs-gated populations were subjected to bulk population RNA-seq alongside CD206^{-}MHC^{lo}F4/80^{hi} TAMs as a comparator group. Principal component (PC) analysis confirmed these populations to be transcriptionally distinct (Fig. 2G). Comparing the bulk population RNA-seq to that of the scRNA-seq populations validated close concordance between the identified populations across a range of predicted marker genes (Fig. 2H). Lyve-1^{+} TAMs also selectively expressed the transcription factor *Maf* (fig. S2D) and CD206^{int}MHCII^{hi}Lyve-1^{-} the transcription factor *Retnla* (Fig. 1D), which may indicate that these transcription factors play a role in polarization identity.

Lyve-1 has traditionally been considered a marker of lymphatic endothelium (*29*), but has also been utilized as a marker on tissue-resident macrophages (*30-35*) and TAMs (*36*). It has been demonstrated that macrophages expressing Lyve-1 can be found to spatially reside proximal to vasculature (*34*) and, indeed, immunofluorescence staining of tissue

sections from *MMTV-PyMT* tumors confirmed Lyve-1$^+$ TAMs to be a population of perivascular cells (Fig. 2I). As Lyve-1 expression can be found on macrophages in homeostatic tissues (*30-35*), we investigated whether an equivalent macrophage population could be identified in the mammary gland prior to tumor onset. Using the flow cytometry gating strategy of Franklin et al (*22*) for mammary tissue macrophages, an equivalent macrophage population (based on CD206 and MHCII markers) could not be found in the mammary gland prior to tumor onset (fig. S3A). Although, a population of Lyve-1$^+$ macrophages does reside in the mammary gland, its phenotype is distinct from that of Lyve-1$^+$ TAM population, most notably in a lower expression of CD206 (fig. S3A,B). Although this study does not rule out a direct link between Lyve-1$^+$ macrophages in the mammary gland and the TAM population that arises in the tumor, their exact origin remains to be determined. However, these data do at least suggest that the phenotype of Lyve-1$^+$ TAMs has been polarized by the tumor microenvironment. GO pathway analysis also suggested that Lyve-1$^+$ TAMs were highly endocytic (Fig. 2C). Liposomes containing the fluorescent lipophilic dye 1'-dioctadecyl-3,3,3',3''tetramethylindocarbocyanine perchlorate (Dil) have previously been used to study perivascular TAM (pvTAM) development (*19*) and we predicted they could represent a tool to preferentially label the Lyve-1$^+$ TAM subset. We developed a labeling protocol that could selectively mark pvTAMs. Confocal analysis of the labeled tumors demonstrated that Dil-liposomes specifically labeled a population of pvTAMs (Fig. 2J-M and fig. 4A-C) and *ex vivo* characterization of the Dil-labeled TAMs in enzyme-dispersed tumors confirmed the vast majority of labeled cells to be that of the Lyve-1$^+$ TAM subset (Fig. 2M).

As the liposome labeling protocol preferentially labeled Lyve-1$^+$ TAMs (Fig. 2M and fig. S4B-C), we utilized clodronate-filled liposomes (*37*) under an equivalent administration protocol as a means to selectively deplete the population and investigate their possible role in tumor progression. Depletion of these cells in *MMTV-PyMT* tumors resulted in a significant slowing of tumor growth (Fig. 3A,B), highlighting a fundamental role for these cells in tumor progression. Even over the long-term administration of clodronate-filled liposomes, which displayed little sign of toxicity in the animals (fig. S4D), provided a preferential depletion of Lyve-1$^+$ TAMs, sparing CD206$^-$ and CD206$^-$MHCII^{hi} TAM populations (Fig. 3C,D), and CD11b$^+$Ly6C$^+$ monocytes (Fig. 3E). Furthermore, using immunofluorescence imaging there was an observable selective spatial loss of perivascular TAMs (pvTAMs) within the clodronate-filled liposome treated mice (Fig. 3F), where the majority of TAMs surrounding blood vessels were no longer observable. To understand the mechanism through which Lyve-1$^+$ pvTAMs promote tumor progression (Fig. 3B), we first phenotyped the immune-infiltrate of the tumors. Loss of Lyve-1$^+$ pvTAMs did not change the abundance of any immune cell populations analyzed within the tumor microenvironment, other than a

statistically significant increase in the abundance of the migratory CD11c^{+}CD103^{+}dendritic cells (DCs) (Fig. 3G and fig. S4E), which contribute to cytotoxic T-lymphocyte recruitment in the tumor (*38*) and priming of the anti-tumor immune response (*39*). However, there was no increase in CD8^{+} or CD4^{+} T-cell recruitment post depletion of Lyve-1^{+} pvTAMs (Fig. 3G). Perivascular macrophages are known to play a role in angiogenesis (*6*), and the Lyve-1^{+} pvTAM population expressed pathways associated with pro-angiogenic functions (Fig. 2C), which could account for the control of tumor growth observed when the TAM subset was depleted (Fig. 3B). Immunofluorescence analysis of these tumors had shown no overall change in density of endothelial cells within the tumor (Fig. 3H,I), but the tumors themselves were smaller (Fig. 3B). Further analysis of sections from *MMTV-PyMT* tumors stained for CD31^{+} endothelial cells and perivascular α-smooth muscle actin (αSMA) expressing stromal cells revealed a change in vessel architecture, where depletion of Lyve-1^{+} pvTAMs resulted in an increase in the number of individual vessel elements in the tumor (Fig. 3J) with the vessel elements appearing smaller and less branched (Fig. 3K). However, most strikingly, there was a loss of αSMA^{+} stromal cells proximal to vasculature (Fig. 3H,L). Although there is evidence that fibroblasts can be phagocytic (*40*), neither CD45^{-}CD90^{+} CAFs (*41*) nor CD45^{-} or CD31^{+} endothelial cells had up-taken the liposomes (fig. S4B), excluding any direct killing effect of the clodronate on these populations and highlighting a potential role of Lyve-1^{+} pvTAMs in maintaining this stromal population.

Staining tissue sections from *MMTV-PyMT* tumors for the αSMA^{+} cells and F4/80^{+} TAMs placed these populations in a close spatial arrangement with CD31^{+} vasculature providing opportunity for interactions and suggested a 'niche' formation (Fig. 4A). The median distance between αSMA^{+} cells and F4/80[+] TAMs was only 20±7 µm (less than a cell thickness) highlighting the close association between these cells (Fig. 4B). A similar niche was also found in human invasive breast cancer (Fig. 4C), where 44.7±10.2% of TAMs could be found in a perivascular niche with αSMA^{+} cells and 8.4±3% TAMs could be found in direct contact with αSMA^{+} cells (Fig. 4D). This immune-mesenchymal niche was not present within ductal carcinoma *in situ* (DCIS) tissue (Fig. 4C) but could be found around the vessels in the adjacent tissue (albeit at a lower abundance than found within the tumor; fig. S5A-B). Lyve-1^{+} macrophages have been identified in healthy tissue in close proximity to αSMA-expressing smooth muscle cells in the mouse aorta where they play a homeostatic functional role in modulating collagen production which influences arterial tone (*35*). To further investigate these perivascular Lyve-1^{+} TAM-dependent αSMA^{+} cells in our preclinical model of cancer, we characterized the heterogeneity of a broad pool of tumor-associated mesenchymal stromal cells (collectively termed cancer associated fibroblasts; CAFs) using flow cytometry within enzyme-dispersed *MMTV-PyMT* tumors. The CD45^{-}CD31^{-}CD90^{+}

population accounted for 4.0±1.6% of total live cells within 350mm^3 tumors and their abundance increased as tumors progressed (Fig. 4E). We screened the CD45$^-$CD90$^+$ population for cell surface markers associated with mesenchymal subsets, including; Ly6a, CD34, PDGFRα, FAP and CD29 (*41-45*). Clustering of the multi-parametric flow cytometry data using *UMAP* (*24*) and *FlowSOM* (*46*) distinguished two distinct subsets (Fig. 4F). The first subset 'CAF1' was CD29^{hi}CD34$^-$Ly6a$^-$FAP^{lo}PDGFRα^{lo} and the second 'CAF2' was CD29^{lo}CD34$^+$Ly6a$^+$FAP^{hi}PDGFRα^{hi} (Fig. 4F). Although the two subsets of CAFs could have been separated based on any of the markers utilized, the two populations were FACs-sorted based on their differing expression of CD34 for bulk RNA-seq to confirm the αSMA-expressing population (fig. S5C). CD34 was selected to separate these CAF subsets and has been previously demonstrated to negatively correlate with αSMA expression in CAFs in models of pancreatic adenocarcinoma (*47*). This analysis demonstrated clear transcriptional differences in these subsets (Fig. 4G and fig. S5D-E). The CD34$^+$ CAF population was functionally more skewed towards inflammation-related processes, while the CD34$^-$ CAF displayed an extracellular matrix (ECM) and pro-angiogenesis related-program (Fig. 4G-H and fig. S5E). The CD34$^-$ CAF population also selectively expressed high levels of αSMA (*Acta2*) (Fig. 4I). These CAF subsets were largely similar to those identified in pancreatic ductal adenocarcinoma (PDAC) (*42*), however there were also key differences such as *Il6* was not a discriminatory marker for the CAF populations in *MMTV-PyMT* tumors (Fig. 4J). Interestingly, the CD34$^-$ CAF population also expressed *Des, Pdgfrb* and *Cspg4* (Fig. 4K) which are genes that are often associated with pericytes, a population of specialized vessel-associated cells (*48, 49*). To confirm the presence of pericyte markers desmin (*Des*), PDGFRβ (*Pdgfrb*) and NG2 (*Cspg4*) at the protein level in these cells, immunofluorescence staining of tissues sections from *MMTV-PyMT* mice confirmed that the perivascular αSMA$^+$ cells also were desmin$^+$ (fig. S5F), and *ex vivo* flow cytometry confirmed the presence of surface PDGFRβ (fig. S5G) and NG2 (fig. S5H). CD34$^-$ CAFs expressed PDGFRα, albeit low relative to the CD34$^+$ population (Fig. 4F and fig. S5G), which is regarded as a broad marker of fibroblasts. The pericyte marker NG2 and fibroblast marker PDGFRα colocalized at the protein level on the CD34$^-$ CAFs, where higher NG2 expression was associated with relatively higher PDGFRα expression within the population (fig. S5H), suggesting the population may represent either a 'pathological' pericyte phenotype or a pericyte-like CAF population. Pericytes are important to angiogenesis, supporting vessel stabilization and endothelial cell survival (*50*). The CD34$^-$ CAF population also displays similarities in gene expression to vasculature-associated 'vCAFs*'* recently characterized in *MMTV-PyMT* tumors, although vCAFs did not have detectable surface protein expression of NG2 (*45*). A phenotypically similar pericyte-like CAF population expressing CD29, PDGFRβ and high levels of αSMA, has also been identified in human breast cancer (*43*). Heterogeneous

expression of CD34 differentiated CAF populations across different ectopic tumor models including B16, LL2 and orthotopic 4T1 (fig. S5I,J). Due to αSMA representing a defining feature of these cells we elected to refer to these cells herein as 'αSMA⁺ CAFs'. Analyzing the abundance of the CAF populations over the different stages of tumor progression from the healthy mammary gland, hyperplasia and the growing tumor revealed a relative increase in the abundance of the αSMA⁺ CAFs within the broader CAF population over tumor progression, suggesting a preferential selection of this subset within the tumor microenvironment (Fig. 5A). To elucidate the route through which these cells were accumulating in the tumor, we first explored local proliferation and pulsed mice bearing *MMTV-PyMT* tumors with 5-ethynyl-2'-deoxyuridine (Edu) to label actively proliferating cells. Although both CD34⁺ CAF and αSMA⁺ CAF populations displayed evidence of proliferation by comparison with healthy mammary gland, the αSMA⁺ CAFs were proliferating at a significantly faster rate (Fig. 5B). To address whether the proliferation was sufficient to account for their preferential expansion with tumor growth we utilized the *Kaede* mouse (*51*) crossed to the *MMTV-PyMT* model. Using this approach, we were able to photoconvert all tumor and stromal cells within a 100mm³ tumor from *Kaede*-green to *Kaede*-red (Fig. 5C). Analyzing tumors 72h after photoconversion demonstrated that CD45⁺ stromal cells predominantly displayed *Kaede*-green, highlighting the continual recruitment of hematopoietic stromal cells to the tumor from the periphery (*19, 22*). In contrast, both CD34⁺ CAFs and αSMA⁺ CAF populations remained *Kaede*-red, which indicated that both CAF populations derived from a tumor-resident source of cells and was not dependent on recruitment (Fig. 5C). Therefore, the rapid proliferation of the αSMA⁺ CAFs relative to CD34⁺ CAFs may also contribute to the dynamics of CAF heterogeneity over tumor growth (Fig. 5A).

Immunofluorescence analysis for Ki67, a marker of proliferation (*52*), on αSMA⁺ cells, which we had identified as perivascular, confirmed a close spatial relationship between proliferating Ki67⁺αSMA⁺ CAFs and F4/80⁺ TAMs (Fig. 5D), which were a median distance of 22.6±8.5 μm (within a cell thickness) from each other (Fig. 5E). To investigate whether Lyve-1⁺ pvTAMs might be implicated in the expansion of αSMA⁺ CAFs, we analyzed the incorporation of Edu after the depletion of Lyve-1⁺ pvTAMs using clodronate-filled liposomes (Fig. 5F,G). Despite no observable drop in the proportion of αSMA⁺ CAFs within the tumor over the short-term acute treatment regimen (Fig. 5H), depleting Lyve-1⁺ pvTAMs significantly diminished the high rate of proliferation of the αSMA⁺ CAF population (Fig. 5I). Conversely, the proliferation rate of the CD34⁺ CAF and tumor cell compartments remained unaffected by the loss of Lyve-1⁺ pvTAMs (Fig. 5I).

To resolve how Lyve-1$^+$ pvTAMs could be orchestrating αSMA$^+$ CAF expansion within the perivascular niche, we utilized *CellPhoneDB*, a manually curated repository and computational framework to map the possible biological ligand:receptor interactions within RNA-seq datasets (*53*) between the Lyve-1$^+$ pvTAMs, αSMA$^+$ CAFs and CD31$^+$ endothelial cells (which were all bulk-population RNA-sequenced) to construct an interactome of the major cell types in the perivascular niche (Fig. 6A). There were a total of 653 possible unique ligand:receptor interactions between these three cell types, highlighting the range of potential crosstalk between these populations in constructing the perivascular niche (fig. S6A). To refine this list, we selected for known mitogenic non-integrin mediated ligands which were enriched in Lyve-1$^+$ pvTAMs compared to other TAM populations and could interact with receptors specifically expressed on αSMA$^+$ CAFs and not endothelial cells (Fig. 6B,C). This highlighted the selective crosstalk between these two proximal cells involving *Pdgfc* (*54*) expressed by the Lyve-1$^+$ pvTAMs signaling to *Pdgfra* on the αSMA$^+$ CAFs within the perivascular niche (Fig. 6C). More broadly, the Lyve-1$^+$ TAM subset was a major source of *Pdgfc* in the tumor (Fig. 6D and S6B) and Lyve-1$^+$ TAMs could be found expressing PDGF-C in the perivascular niche (Fig. 6E).

PDGFRs form either homo- or hetero-dimers between the α and β receptor subunit (αα, αβ and ββ) and a homodimer of PDGF-C (PDGF-CC) selectively signals through PDGFRαα and PDGFRαβ dimers (*55*) which has been demonstrated to be a mitogenic and migratory factor for human dermal myofibroblasts (*56, 57*). In an elegant series of *in vitro* studies, macrophages have been demonstrated to form close stable homeostatic 'circuits' with fibroblasts through their secretion of PDGF-BB as a means to maintain relative cell number (*58*). In cancer such circuits, which rely on contact between the macrophage and fibroblast (*58*), could underpin the expansion of the perivascular niche due the continual recruitment of monocytes to the tumor allowing a reciprocal expansion of the fibroblast population in the niche environment. To assess whether PDGF-CC may play a role in orchestrating the expansion of the αSMA$^+$ CAF population within the perivascular niche we administered neutralizing antibodies to PDGF-CC (*57*), within an acute treatment regimen, in tumor bearing *MMTV-PyMT* mice (Fig. 6F). Neutralization of PDGF-CC did not affect the abundance of the cell populations at the acute timepoint (Fig. 6G) but did diminish Edu$^+$ incorporation of the αSMA$^+$ CAFs, but not in the tumor cells or CD45$^-$CD31$^+$ endothelial cells within the vascular niche (Fig. 6H). This highlighted that the expansion of perivascular αSMA$^+$ CAFs was PDGF-CC dependent and could account for the role of Lyve-1$^+$ pvTAMs in orchestrating expansion of the population during tumor progression. As a population of perivascular fibroblasts have been implicated in recruiting macrophages to the perivascular niche (*19*), these observations in the current study highlight a potential reciprocal

interactions between TAMs and mesenchymal populations in perivascular niche formation. PDGF-CC is a prognostic factor for poor survival in breast cancer (*59*) and has been demonstrated to be important to angiogenesis (*60, 61*). Within the perivascular niche the αSMA+ CAFs selectively expressed PDGFRα (Fig. 6I,J), alongside PDGFRβ (fig. S5G), and as such, were the only cell to be capable of responding to PDGF-CC. Tumors grow slower in *MMTV-PyMT Pdfgc-/-* mice and display increased necrotic areas and evidence of hemorrhage (*59*). In accordance with our observations in murine models, using The Cancer Genome Atlas (TCGA) we observed an enrichment for a αSMA+ CAF signature (using genes identified in the murine population) above that of healthy tissue in human breast cancer (fig. S6C) and interestingly the αSMA+ CAF signature also positively correlated with *PDGFC* expression within the tumor (fig. S6D). This study raises an interesting parallel to the observations by Shook et al., that macrophages expressing PDGF-CC support the expansion of αSMA+ myofibroblast populations in the wound healing response (*57*), a stromal response which share many similarities to that of cancer (*4, 62*).

This study characterizes a biologically important subset of TAMs selectively expressing Lyve-1. We demonstrate that the Lyve-1+ pvTAM subset, which only accounts for 1.4±0.4% of live tumoral cells, is pivotal to tumor growth. We define a new role for pvTAMs in directing the expansion of a perivascular pericyte-like mesenchymal population to form a pro-angiogenic niche that is facilitated by a selective PDGFRα:PDGF-CC crosstalk (Fig. 6K). This study highlights the inter-reliance of stromal populations and the importance of the immune system in orchestrating non-immune stromal cell reactions in cancer which provides therapeutic opportunities for unraveling the complexity of the stromal support network and niches which underpin tumor progression.

Materials and Methods

Mice

MMTV-PyMT (*PyMT*) mice used in this study were on an FVB/N background. Balb/c and C57Bl/6 wild type mice were obtained from Charles River. Female C57Bl/6 homozygous *Kaede* mice (*51*) were crossed with male *MMTV-PyMT* (FVB background) mice and the F1 offspring used experimentally. Cohort sizes were informed by prior studies (*4, 14*). All mice used for experiments were female and randomly assigned to treatment groups. Mice were approximately 21-26 g when tumors became palpable. Experiments were performed in at least duplicate and for spontaneous *MMTV-PyMT* tumor studies individual mice were collected on separate days and all data points are presented.

Tumor studies

Murine 4T1 mammary adenocarcinoma, Lewis lung carcinoma (LL2) and B16-F10 melanoma cells were obtained from ATCC. 2.5 x 10^5 cells in 100µl RPMI and were injected by subcutaneous (s.c.) injection into the mammary fat pad of syngeneic Balb/c (4T1) or C57Bl/6 (B16-F10 and LL2) female mice that were six to eight weeks of age. In studies using *MMTV-PyMT* mice tumors arose spontaneously. When tumors became palpable, volumes were measured every 2 days using digital caliper measurements of the long (L) and short (S) dimensions of the tumor. Tumor volume was established using the following equation: Volume= $(S^2xL)/2$. *PyMT/Kaede* mice were photo-labeled under anesthesia, individual tumors mice were exposed to a violet light (405nm wavelength) through the skin for nine 20 second exposure cycles with a short 5 second break interval between each cycle. Black cardboard was used to shield the rest of the mouse throughout the photoconversion procedure. Mice for 0 h time points were culled immediately after photoconversion. This photoconversion approach was adapted from that used to label peripheral lymph nodes (*63*). Tumor tissue for flow cytometry analyses were enzyme-digested to release single cells as previously described (*41*). In brief, tissues were minced using scalpels, and then single cells were liberated by incubation for 60 mins at 37°C with 1 mg/ml Collagenase I from *Clostridium Histolyticum* (Sigma-Aldrich) and 0.1 mg/ml Deoxyribonuclease I (AppliChem) in RPMI (Gibco). Released cells were then passed through a 70 µm cell strainer prior to staining for flow cytometry analyses. Viable cells were numerated using a hemocytometer with trypan blue (Sigma-Aldrich) exclusion. For drug treatments, drugs were freshly prepared on the day of injection and administered by intraperitoneal (i.p.) injection using a 26 G needle. For EdU experiments mice were injected i.p. with 50 mg/kg EdU dissolved in Dulbecco's phosphate buffered saline (PBS) and sacrificed 4 hours post-injection. To liposome deplete Pv macrophages, *MMTV-PyMT* mice were injected i.p. with 150 µl of either clodronate- or PBS-filled liposomes (Anionic Clophosome, FormuMax) on the indicated days. To label PvTAM, *MMTV-PyMT* mice were injected i.p. with 150 µl of Dil fluorescent tracing liposomes (Anionic Clophosome, FormuMax). To neutralize PDGF-CC, we used an antibody which has previously been used *in vivo* to block PDGF-CC signaling (*57*), mice were injected i.p. with 100 µg of a goat anti-PDGF-C neutralizing antibody (AF1447, Bio-techne) solubilized in PBS on day -2 and -1 prior to analysis.

Murine tissue staining

Mouse mammary tumors were fixed overnight (O.N.) in 4% paraformaldehyde, followed by O.N. dehydration in 30% sucrose prior to embedding in OCT and snap freezing in liquid nitrogen. Frozen sections from these tumors were fixed in 4% paraformaldehyde in PBS for 10 mins at RT and were washed in Tris Buffered Saline (100mM Tris, 140mM NaCl), 0.05%, Tween 20, pH7.4 (TBST) and blocked with TBST, 10% donkey serum (Sigma-Aldrich), 0.2% Triton X-100. Immunofluorescence was performed as previously described (*4*). Antibodies and dilutions against the following targets were used: F4/80 1:100 (C1:A3-1, Bio-RAD), αSMA 1:100 (AS-29553, Anaspec), CD31 1:100 (MEC13.1, Biolegend), CD31 1:100 (ab28364 Abcam), mKi67 1:100 (AF649, R&D Systems), CD34 1:100 (RAM34, Invitrogen), desmin 1:100 (PA5-19063, Invitrogen), PDGF-C 1:100 (AF1447 R&D Systems). Primary antibodies were detected using antigen specific Donkey IgG, used at 1:200: AlexaFluor® 405 anti-rabbit IgG, AlexaFluor® 488 anti-rabbit IgG, AlexaFluor® 488 anti-rat IgG, AlexaFluor® 568 anti-rabbit IgG, AlexaFluor® 568 anti-goat IgG, AlexaFluor® 647 anti-rabbit IgG (Thermo Fisher Scientific), NL657 anti-rat goat IgG (R&D) and Cy3 anti-sheep donkey IgG (Jackson Immuno) were also used. Viable blood vessels were visualized in mice through i.v. injection of FITC-conjugated dextran (MW20,000, Thermo Fisher Scientific) 20 min prior to sacrifice. Nuclei were stained using 1.25 µg/ml 4',6-diamidino-2-phenylindole,dihydrochloride (DAPI) (Thermo Fisher Scientific). Images were acquired using a Nikon Eclipse Ti-E Inverted spinning disk confocal with associated NIS Elements software. Quantitative data was acquired from the images applied to Figure 2 and was generated using NIS Elements.

For quantitative data generated for murine tissue staining in Fig. 4, a CellProfiler v3.0 (*64*) pipeline was used to identify cells as DAPI+ 'primary objects' (i.e. all cells) via thresholding analysis. TAM and CAF DAPI+ 'secondary objects' were then generated by cell surface and cytoplasmic staining of the protein markers F4/80 and αSMA, respectively. XY location and nuclear Ki67 staining status of the identified CAF and TAM object data was exported from the CellProfiler pipeline and nearest neighbor identification was carried out using the FNN R package https://CRAN.R-project.org/package=FNN.

Human tissue staining

FFPE human breast adenocarcinoma tissue sections of 4 µm were incubated at 60°C for 1 h, before being deparaffinized with Tissue-Tek® DRS™2000, Sakura. Heat-induced antigen retrieval was performed using a pressure cooker (MenaPath Access Retrieval Unit, PASCAL). The slides were immersed in modified citrate buffer pH 6 and gradually heated to

125°C. Excess of antigen retrieval buffer was washed firstly with distilled water followed by PBS, before incubation of the slides in blocking buffer containing 0.5% Triton and 5% donkey serum (Sigma) for 30 mins at room temperature. The sections were then probed with anti-CD68 1:100 (KP1, Invitrogen), anti-αSMA 1:200 (1A4, Sigma-Aldrich) and anti-CD31 1:100 (EP3095, Abcam) diluted in blocking buffer overnight at 4°C. After further washing, sections were stained for 2 h with donkey IgG antibodies purchased from Jackson Immunoresearch and used at 1:600; AlexaFluor® 647 anti-mouse IgG and AlexaFluor® 488 anti-rabbit IgG. After washing in PBS, the sections were incubated with anti-αSMA conjugated with CY3 probe 1:200 (1A4, Sigma-Aldrich). Counterstaining was performed with 1:2000 DAPI (Cell Signalling Technology) for 5 mins, followed by a wash step using PBS. Mounting medium (Fluorsave, Millipore) was applied to the slides. Images were acquired using a Nikon Eclipse Ti-E Inverted spinning disk confocal with associated NIS Elements software or Olympus slide scanner VS120-S6-W. VSI (Olympus) images were analyzed using VisioPharm analysis software. Briefly, regions of interest (ROIs) were drawn manually to select all areas containing tumor (DCIS and/or invasive breast cancer) in each image. Subsequently, a threshold algorithm-based Application Protocol Package (APP) was developed. Threshold classification method was based on custom defined input bands (FITC, CY3 and CY5). This APP allowed to segment the original image, based on the expression of the pre-defined markers. Post-processing steps were added to the APP to remove noise, to better define the vasculature co-expressing CD31 and αSMA markers, and to distinguish between PvTAMs, located within 50 µm radius from the vascular structures and the rest of the macrophages.

Flow cytometry

Flow cytometry was performed as previously described (*1*). The following antibodies against the indicated antigen were purchased from Thermo Fisher Scientific and were used at 1 µg/ml unless stated otherwise: CD3ε APC and PE (145-2C11), CD4 FITC (RM4-5), CD8β eFluor®450 (H35-17.2), CD11b APC-eFluor®780 (M1/70), CD11b BV510 (M1/70), CD11c APC (N418), CD16/32 (2.4G2; Tonbo Biosciences), CD19 APC (6D5; Biolegend®), CD29 APC (eBioHMb1-1), CD31 eFluor® 450 and PE (390), CD34 FITC and APC (RAM34), CD45 APC-eFluor®780, FITC and PerCP-Cy5.5 (30-F11), CD90.2 eFluor® 450 (53-2.1), CD90.1 eFluor® 450 (HIS51), CD90.1 BV510 (OX-7), CD103 PE (2E7), CD206 APC (FAB2535A; Bio-Techne), F4/80 PE (BM8; Biolegend®), F4/80 BV421 (BM8; Biolegend®), FAP (10 µg/ml, AF3715, Bio-Techne), Ly6C PE and eFluor® 450 (HK1.4), Ly6G FITC (1A8; Biolegend®), Lyve-1 AlexaFluor® 488 (ALY7), MHCII PE, FITC and eFluor® 450 (M5/114.15.2), NG2

AlexaFluor® 488 (AB5320A4; Millipore) NK1.1 APC (PK136), PDGFRα APC and PerCP-Cy5.5 (APA5), PDGFRβ PE (APB5), Ly6A/E AlexaFluor® 700 (D7). Where stated, the following corresponding isotype control antibodies at equivalent concentrations to that of the test stain were used: Armenian Hamster IgG APC (eBio299Arm), goat IgG APC and PE (Bio-techne), rat IgG2a APC, PE and FITC (eBR2a) and rat IgG2b APC and eFluor® 450 (eB149/10H5). Intracellular stains were performed as previously described (1). Dead cells and red blood cells were excluded using 1 µg/ml 7-amino actinomycin D (7AAD; Sigma-Aldrich), Fixable Viability Dye eFluor® 780 (Invitrogen) or DAPI alongside anti-Ter-119 PerCP-Cy5.5 or APC-eFluor® 780 (Ter-119; Invitrogen). The FAP primary antibody was detected with a secondary biotin-conjugated anti-goat/sheep mouse IgG and 1:1000 Streptavidin PE-Cy7 (Thermo Fisher Scientific). EdU was detected using the Click-IT Plus Flow Cytometry Assay with AlexaFluor® 488 (Thermo Fisher Scientific) in accordance with the manufacturers' specifications. Briefly, cells were stained with cell surface antibodies and then fixed and permeabilized and the click chemistry reaction was performed as specified with AF488-conjugated Picolyl Azide to identify EdU incorporated into the genomic DNA. Cells were sorted to acquire pure populations using a FACS Aria (BD Biosciences). Data were collected on a BD FACS Canto II (BD Biosciences) or a BD LSR Fortessa (BD biosciences). Data was analyzed using FlowJo software (BD biosciences). Unsupervised clustering of flow cytometry data was performed using the *ImmunoCluster* package (65). Briefly, the single-cell data was asinh transformed with cofactor of 150 and clustering was performed with and ensemble method using *FlowSOM* (46) and ConsensusClusterPlus (66) to k=8 clusters, based on the elbow criterion, which were manually merged based on expression profiles into biologically meaningful populations as previously outlined (67). Dimensionality reduction for visualization purposes was performed with *UMAP* (24).

Quantitative real time quantitative PCR

mRNA was extracted from FACS-sorted cell populations using the Trizol method and converted to cDNA/amplified using the CellAmp™ Whole Transcriptome Amplification Kit (Real Time), Ver. 2 kit (Takara) according to the manufacturer's protocol. mRNA of interest was measured using the SuperScriptTM III PlatinumTM One-Step qRT-PCR Kit (Thermo Fisher Scientific) according to the manufacturer's protocol with the primers/probes *Actb* Mm02619580_g1 and *Pdgfc* Mm00480295_m1 (Thermo Fisher Scientific). Expression is represented relative to the housekeeping gene *Actb*. Gene expression was measured using an ABI 7900HT Fast Real Time PCR instrument (Thermo Fisher Scientific).

Single-cell RNA-sequencing

TAMs (CD45+Ly6G-CD11b+F4/80hi) were sorted from enzyme-digested *MMTV-PyMT* tumors and a total of 10,502 TAMs were sequenced from three *MMTV-PyMT* tumors and run through the 10x Genomics Chromium platform. An average of 43k reads per cell, a median of 2,400 genes and median UMI count of 9,491 per cells was obtained. Single-cell suspensions were prepared as outlined in the 10x Genomics Single Cell 3' V3 Reagent kit user guide (10x Genomics). Briefly, samples were washed with PBS (Gibco) with 0.04% bovine serum albumin (Sigma-Aldrich) and resuspended in 1 ml PBS, 0.04% BSA. Sample viability was assessed using trypan blue (Thermo Fisher Scientific) exclusion and an EVE automated cell counter (Alphametrix) in duplicate, in order to determine the appropriate volume for each sample to load into the Chromium instrument. The sorted TAMs were loaded onto a Chromium Instrument (10x Genomics) to generate single-cell barcoded droplets according to the manufacturers' protocol using the 10x Genomics Single Cell 3' V3 chemistry. cDNA libraries were prepared as outlined by the Single Cell 3′ Reagent kit v3 user guide and each of the three resulting libraries were sequenced on one lane each of a HiSeq 2500 (Illumina) in rapid mode.

Single-cell RNA-sequencing data processing and analysis

The raw sequenced data was processed with the Cell Ranger analysis pipeline version 3.0.2 by 10x Genomics (http://10xgenomics.com/). Briefly, sequencing reads were aligned to the mouse transcriptome mm10 using the STAR aligner (*68*). Subsequently, cell barcodes and unique molecular identifiers underwent Cell Ranger filtering and correction. Reads associated with the retained cell barcodes were quantified and used to build a transcript count tables for each sample. Downstream analysis was performed using the Seurat v3 R package (*69*). Before analysis, we first performed quality control filtering with the following parameters: cells were discarded on the following criteria: where fewer than 800 unique genes detected, reads composed greater than 12% mitochondrial-associated gene transcripts and cells whose number of reads detected per cell was greater than 65k for sample 1 and 2, 60k for sample 3. All genes that were not detected in at least ten single cells were excluded. Based on these criteria the final dataset contained 9,615 TAMs with 25,142 detected genes. The data was first normalized using the LogNormalize function and a scale factor of 10,000. The 2,000 genes with highest variance were selected with the FindVariableGenes function. In order to minimize the effect of cell cycle associated genes in the dimensionality reduction and clustering, cell cycle associated genes defined by the GO term 'Cell Cycle' were removed from the variable gene dataset resulting in 1,765 variable

genes. Principal component (PC) analysis was used on the highly variable genes to reduce the dimensionality of the feature space and 35 significant PCs were selected for downstream analysis. To reduce biases caused by technical variation, sequencing depth and capture efficiency, the three sequencing samples were integrated using the Seurat integration method (*69*) as specified. Clusters were identified by a graph based SNN clustering approach within Seurat using the resolution parameters 0-1 in steps of 0.1, followed by analysis using the Clustree R package (*70*). Finally, we used resolution parameter of 0.4 to define 10 clusters. Differentially expressed genes were identified using the FindAllMarkers function where the genes must be detected in a minimum of 25% of cells and have a logFC threshold of 0.25. After identifying marker genes, we excluded two clusters which contained suspected contaminating epithelial cells (enriched in *Epcam*, *Krt18*, *Krt8*) and dying low-quality cells (enriched in mitochondrial genes and ribosomal subunit genes). Ultimately, we identified 8 relevant clusters. All gene scores were calculated from the integrated Seurat data object where the data was scaled using the scaleData () function across all TAM transcriptomes. The genes composing the M1 and M2 gene scores were derived from Orecchioni et al (*27*), specifically from Supplemental Table 1. Genes present in the gene signatures that were not detected by any cells in the dataset were discarded. The gene score was calculated per cell as the mean of the scaled gene expression across of the M1 or M2 associated genes and the individual cell gene scores are plotted grouped by TAM cluster. We used the Slingshot R package (*25*) to investigate inferred polarization trajectories in our TAM population. Briefly, dimensionality reduction was performed using diffusion maps with the Destiny R package (*71*) using the significant PCA principal components used for clustering. A lineage trajectory was mapped into the diffusion space using the first 15 diffusion components (DCs) by Slingshot and each cell was assigned a pseudotime value based on its predicted position along the predicted trajectories. We selected the cluster TAM01 as the base state for the trajectory because it had the lowest M1/M2 activation-associated gene score amongst the terminal trajectory branch clusters, no discriminating upregulated GO pathways and the fewest differentially expressed genes and represented the most naïve TAM transcriptomic base state. To detect non-linear patterns in gene expression over pseudotime trajectory, we used the top variable gene set and regressed each gene on the pseudotime variable we generated, using a general additive model (GAM) with the GAM R package (CRAN - Package gam (r-project.org). Heatmaps were generated with the ComplexHeatmap package (*72*).

Bulk RNA-sequencing

Cells were sorted directly into RLT plus buffer (Qiagen) supplemented with 2-β-mercaptoethanol (BME) (Gibco) and lysates were immediately stored at -80°C until used. RNA was extracted with the RNeasy Plus Micro kit (Qiagen) as per the manufacturers' protocol, in addition to on-column DNase digestions specified by the manufacturer (Qiagen). cDNA was generated and amplified using the SMARTseq v4 Ultra Low Input RNA Kit (Clontech) on the contactless Labcyte liquid handling system (Beckman Coulter Life Sciences). Two hundred ng of amplified cDNA was used from each sample where possible to generate libraries using the Ovation Ultralow Library System V2 kit (NuGEN). In brief, cDNA was fragmented through sonication on Covaris E220 (Covaris Inc.), repaired, and polished followed by ligation of indexed adapters. Adapter-ligated cDNA was pooled before final amplification to add flow cell primers. Libraries were sequenced on HiSeq 2500 (Illumina) for 100 paired-end cycles in rapid mode.

Bulk RNA-sequencing data processing and analysis

Pre-alignment QC for each sample, independently for forward and reverse reads, was performed using the standalone tool FastQC. Reads were trimmed using Trimmomatic (*73*) and aligned to the reference genome (mm10) using HISAT2 (*74*). PCR duplicates were removed using SAMtools (*75*). Counts were generated using the GenomicAlignment (*76*) package using the mm10 reference genome. Prior to performing differential gene expression analysis, genes with very low expression were discarded. Differential expression analysis was performed with DESeq2 (*77*) package in R. The test statistics' p-values were adjusted for multiple testing using the procedure of Benjamini and Hochberg. Genes with adjusted p-values lower than 0.05 and absolute log2 fold change greater than 1 were considered significant. PCA plots were generated using regularized log transformed (rlog) data.

Gene ontology pathway enrichment analysis

Enriched pathways were identified based on cluster (scRNA-seq) or population (bulk RNA-seq) differentially expressed gene lists as input using the web implementation of the gProfiler tool, using the g:GOst module (http://www.biit.cs.ut.ee/gprofiler/). We used pathway gene sets from the 'biological processes' (GO:BP) database of Gene Ontology (http://www.geneontology.org/) to find over-representation of information from the GO terms. All p-values were adjusted for multiple testing using the procedure of Benjamini and Hochberg.

Ligand:receptor mapping analysis

Ligand:receptor mapping was performed with the online implementation of the CellPhoneDB v1.0 tool (https://www.cellphonedb.org/) (*78*) run without the statistical method. Cell type ligand:receptor interactome was generated with each if the five replicates of the sorted cell population derived bulk RNA-seq transcriptomes as input, selecting only genes with expression of 16 normalized counts or greater as input. The resulting interaction list was filtered by selecting non-integrin mediated interactions and TAM ligands that were enriched in the TAM06 scRNA-seq population in the ligand:receptor pairs, finally selecting for ligands present in the GO term 'growth factor activity' that were investigated further as potential candidates.

Computational analysis of cancer patient data

RSEM normalized expression datasets from the Cancer Genome Atlas (TCGA) were downloaded from the Broad Institute Firehose resource (https://gdac.broadinstitute.org/) and analyzed using custom R scripts. The CAF1 gene expression signature was generated by taking the mean normalized log2-transformed expression value of the component signature genes. The CAF1 gene signature genes were selected from the top 25 differentially expressed CAF1 genes by Log Fold change as the maximum set for which a significant positive correlation was observed between all genes and *ACTA2* (αSMA). The final gene set was as follows: *ACTA2, MMP13, LRRC15, COL10A1, SPON1, COL1A1*.

Statistics

Normality and homogeneity of variance were determined using a Shapiro-Wilk normality test and an F-test respectively. Statistical significance was then determined using a two-sided unpaired Students *t* test for parametric, or Mann-Whitney test for nonparametric data using GraphPad Prism 8 software. A Welch's correction was applied when comparing groups with unequal variances. Statistical analysis of tumor growth curves was performed using the "compareGrowthCurves" function of the statmod software package (*79*). No outliers were excluded from any data presented.

Study approval

All experiments involving animals were approved by the Animal and Welfare and Ethical Review Boards of King's College London and the University of Birmingham, and the Home Office UK. Human breast adenocarcinoma tissue was obtained with informed consent under ethical approval from the King's Health Partners Cancer Biobank (REC reference 12/EE/0493).

Data availability

The transcriptomic datasets that support the findings of this study are available through the Gene Expression Omnibus; GSE160561 (bulk RNA-seq) and GSE160641 (scRNA-seq). The authors declare that all other data supporting the findings of this study are available within the paper and its supplementary information files.

Competing interests

Authors declare no competing interests relating to this work.

Author contributions

J.W.O., J.N.A. conceived the project, designed the approach, performed experiments, interpreted the data wrote the manuscript. J.E.A., I.D., E.J.H., I.B., J.C., T.M., P.G., D.S., R.N. designed the approach, performed experiments, and interpreted the data. S.E.P., T.N., F.D., S.K., D.R.W., T.L. designed experiments, interpreted the data and provided key expertise.

References

1. J. N. Arnold, L. Magiera, M. Kraman, D. T. Fearon, Tumoral immune suppression by macrophages expressing fibroblast activation protein-alpha and heme oxygenase-1. *Cancer Immunol Res* **2**, 121-126 (2014).
2. H. Garner, K. E. de Visser, Immune crosstalk in cancer progression and metastatic spread: a complex conversation. *Nature reviews. Immunology* **20**, 483-497 (2020).
3. R. Noy, J. W. Pollard, Tumor-Associated Macrophages: From Mechanisms to Therapy. *Immunity* **41**, 49-61 (2014).
4. T. Muliaditan *et al.*, Macrophages are exploited from an innate wound healing response to facilitate cancer metastasis. *Nature communications* **9**, 2951 (2018).
5. L. Cassetta *et al.*, Human Tumor-Associated Macrophage and Monocyte Transcriptional Landscapes Reveal Cancer-Specific Reprogramming, Biomarkers, and Therapeutic Targets. *Cancer Cell* **35**, 588-602 e510 (2019).
6. C. E. Lewis, A. S. Harney, J. W. Pollard, The Multifaceted Role of Perivascular Macrophages in Tumors. *Cancer Cell* **30**, 365 (2016).
7. B. Qian *et al.*, A distinct macrophage population mediates metastatic breast cancer cell extravasation, establishment and growth. *PLoS One* **4**, e6562 (2009).
8. E. Friebel *et al.*, Single-Cell Mapping of Human Brain Cancer Reveals Tumor-Specific Instruction of Tissue-Invading Leukocytes. *Cell* **181**, 1626-1642 e1620 (2020).
9. L. Zhang *et al.*, Single-Cell Analyses Inform Mechanisms of Myeloid-Targeted Therapies in Colon Cancer. *Cell* **181**, 442-459 e429 (2020).
10. P. J. Murray *et al.*, Macrophage activation and polarization: nomenclature and experimental guidelines. *Immunity* **41**, 14-20 (2014).
11. M. De Palma *et al.*, Tie2 identifies a hematopoietic lineage of proangiogenic monocytes required for tumor vessel formation and a mesenchymal population of pericyte progenitors. *Cancer Cell* **8**, 211-226 (2005).
12. E. Y. Lin *et al.*, Vascular endothelial growth factor restores delayed tumor progression in tumors depleted of macrophages. *Mol Oncol* **1**, 288-302 (2007).

13.   A. Etzerodt *et al.*, Specific targeting of CD163(+) TAMs mobilizes inflammatory monocytes and promotes T cell-mediated tumor regression. *The Journal of experimental medicine* **216**, 2394-2411 (2019).

14.   T. Muliaditan *et al.*, Repurposing Tin Mesoporphyrin as an Immune Checkpoint Inhibitor Shows Therapeutic Efficacy in Preclinical Models of Cancer. *Clinical cancer research : an official journal of the American Association for Cancer Research* **24**, 1617-1628 (2018).

15.   D. G. DeNardo *et al.*, Leukocyte Complexity Predicts Breast Cancer Survival and Functionally Regulates Response to Chemotherapy. *Cancer Discovery* **1**, 54-67 (2011).

16.   J. B. Mitchem *et al.*, Targeting tumor-infiltrating macrophages decreases tumor-initiating cells, relieves immunosuppression, and improves chemotherapeutic responses. *Cancer research* **73**, 1128-1141 (2013).

17.   D. G. DeNardo *et al.*, CD4(+) T cells regulate pulmonary metastasis of mammary carcinomas by enhancing protumor properties of macrophages. *Cancer Cell* **16**, 91-102 (2009).

18.   B. Z. Qian *et al.*, CCL2 recruits inflammatory monocytes to facilitate breast-tumour metastasis. *Nature* **475**, 222-225 (2011).

19.   E. N. Arwert *et al.*, A Unidirectional Transition from Migratory to Perivascular Macrophage Is Required for Tumor Cell Intravasation. *Cell reports* **23**, 1239-1248 (2018).

20.   J. B. Wyckoff *et al.*, Direct visualization of macrophage-assisted tumor cell intravasation in mammary tumors. *Cancer research* **67**, 2649-2656 (2007).

21.   A. S. Harney *et al.*, Real-Time Imaging Reveals Local, Transient Vascular Permeability, and Tumor Cell Intravasation Stimulated by TIE2hi Macrophage-Derived VEGFA. *Cancer Discov* **5**, 932-943 (2015).

22.   R. A. Franklin *et al.*, The cellular and molecular origin of tumor-associated macrophages. *Science* **344**, 921-925 (2014).

23.   C. T. Guy, R. D. Cardiff, W. J. Muller, Induction of mammary tumors by expression of polyomavirus middle T oncogene: a transgenic mouse model for metastatic disease. *Molecular and cellular biology* **12**, 954-961 (1992).

24.   E. Becht *et al.*, Dimensionality reduction for visualizing single-cell data using UMAP. *Nat Biotechnol*, (2018).

25.   K. Street *et al.*, Slingshot: cell lineage and pseudotime inference for single-cell transcriptomics. *BMC Genomics* **19**, 477 (2018).

26.   C. D. Mills, K. Kincaid, J. M. Alt, M. J. Heilman, A. M. Hill, M-1/M-2 macrophages and the Th1/Th2 paradigm. *Journal of immunology* **164**, 6166-6173 (2000).

27.   M. Orecchioni, Y. Ghosheh, A. B. Pramod, K. Ley, Macrophage Polarization: Different Gene Signatures in M1(LPS+) vs. Classically and M2(LPS-) vs. Alternatively Activated Macrophages. *Front Immunol* **10**, 1084 (2019).

28.   J. Boskovic *et al.*, Structural model for the mannose receptor family uncovered by electron microscopy of Endo180 and the mannose receptor. *The Journal of biological chemistry* **281**, 8780-8787 (2006).

29.   D. G. Jackson, R. Prevo, S. Clasper, S. Banerji, LYVE-1, the lymphatic system and tumor lymphangiogenesis. *Trends Immunol* **22**, 317-321 (2001).

30.   S. Ensan *et al.*, Self-renewing resident arterial macrophages arise from embryonic CX3CR1(+) precursors and circulating monocytes immediately after birth. *Nature immunology* **17**, 159-168 (2016).

31.   C. H. Cho *et al.*, Angiogenic role of LYVE-1-positive macrophages in adipose tissue. *Circ Res* **100**, e47-57 (2007).

32.   A. R. Pinto *et al.*, An abundant tissue macrophage population in the adult murine heart with a distinct alternatively-activated macrophage profile. *PLoS One* **7**, e36814 (2012).

33.   H. Xu, M. Chen, D. M. Reid, J. V. Forrester, LYVE-1-positive macrophages are present in normal murine eyes. *Invest Ophthalmol Vis Sci* **48**, 2162-2171 (2007).

34.   S. Chakarov *et al.*, Two distinct interstitial macrophage populations coexist across tissues in specific subtissular niches. *Science* **363**, (2019).

35.   H. Y. Lim *et al.*, Hyaluronan Receptor LYVE-1-Expressing Macrophages Maintain Arterial Tone through Hyaluronan-Mediated Regulation of Smooth Muscle Cell Collagen. *Immunity* **49**, 1191 (2018).

36.   C. Dollt *et al.*, The shedded ectodomain of Lyve-1 expressed on M2-like tumor-associated macrophages inhibits melanoma cell proliferation. *Oncotarget* **8**, 103682-103692 (2017).

37.   A. M. Buiting, F. Zhou, J. A. Bakker, N. van Rooijen, L. Huang, Biodistribution of clodronate and liposomes used in the liposome mediated macrophage 'suicide' approach. *J Immunol Methods* **192**, 55-62 (1996).

38.   S. Spranger, D. Dai, B. Horton, T. F. Gajewski, Tumor-Residing Batf3 Dendritic Cells Are Required for Effector T Cell Trafficking and Adoptive T Cell Therapy. *Cancer Cell* **31**, 711-723 e714 (2017).

39.   E. W. Roberts *et al.*, Critical Role for CD103(+)/CD141(+) Dendritic Cells Bearing CCR7 for Tumor Antigen Trafficking and Priming of T Cell Immunity in Melanoma. *Cancer Cell* **30**, 324-336 (2016).

40.   S. E. Hall, J. S. Savill, P. M. Henson, C. Haslett, Apoptotic neutrophils are phagocytosed by fibroblasts with participation of the fibroblast vitronectin receptor and involvement of a mannose/fucose-specific lectin. *Journal of immunology* **153**, 3218-3227 (1994).

41.   M. Kraman *et al.*, Suppression of antitumor immunity by stromal cells expressing fibroblast activation protein-alpha. *Science* **330**, 827-830 (2010).

42.   D. Ohlund *et al.*, Distinct populations of inflammatory fibroblasts and myofibroblasts in pancreatic cancer. *The Journal of experimental medicine* **214**, 579-596 (2017).

43.   A. Costa *et al.*, Fibroblast Heterogeneity and Immunosuppressive Environment in Human Breast Cancer. *Cancer Cell* **33**, 463-479 e410 (2018).

44.   S. Davidson *et al.*, Single-Cell RNA Sequencing Reveals a Dynamic Stromal Niche That Supports Tumor Growth. *Cell Rep* **31**, 107628 (2020).

45.   M. Bartoschek *et al.*, Spatially and functionally distinct subclasses of breast cancer-associated fibroblasts revealed by single cell RNA sequencing. *Nature communications* **9**, 5150 (2018).

46.   S. Van Gassen *et al.*, FlowSOM: Using self-organizing maps for visualization and interpretation of cytometry data. *Cytometry A* **87**, 636-645 (2015).

47.   C. Feig *et al.*, Targeting CXCL12 from FAP-expressing carcinoma-associated fibroblasts synergizes with anti-PD-L1 immunotherapy in pancreatic cancer. *Proceedings of the National Academy of Sciences of the United States of America* **110**, 20212-20217 (2013).

48.   A. Armulik, G. Genove, C. Betsholtz, Pericytes: developmental, physiological, and pathological perspectives, problems, and promises. *Dev Cell* **21**, 193-215 (2011).

49.   M. Crisan *et al.*, A perivascular origin for mesenchymal stem cells in multiple human organs. *Cell stem cell* **3**, 301-313 (2008).

50.   M. De Palma, D. Biziato, T. V. Petrova, Microenvironmental regulation of tumour angiogenesis. *Nature reviews. Cancer* **17**, 457-474 (2017).

51.   M. Tomura *et al.*, Monitoring cellular movement in vivo with photoconvertible fluorescence protein "Kaede" transgenic mice. *Proceedings of the National Academy of Sciences of the United States of America* **105**, 10871-10876 (2008).

52.   I. Miller *et al.*, Ki67 is a Graded Rather than a Binary Marker of Proliferation versus Quiescence. *Cell reports* **24**, 1105-1112 e1105 (2018).

53.   R. Vento-Tormo *et al.*, Single-cell reconstruction of the early maternal-fetal interface in humans. *Nature* **563**, 347-353 (2018).

54.   X. Li *et al.*, PDGF-C is a new protease-activated ligand for the PDGF alpha-receptor. *Nat Cell Biol* **2**, 302-309 (2000).

55.   D. G. Gilbertson *et al.*, Platelet-derived growth factor C (PDGF-C), a novel growth factor that binds to PDGF alpha and beta receptor. *The Journal of biological chemistry* **276**, 27406-27414 (2001).

56.   M. Jinnin *et al.*, Regulation of fibrogenic/fibrolytic genes by platelet-derived growth factor C, a novel growth factor, in human dermal fibroblasts. *J Cell Physiol* **202**, 510-517 (2005).

57.   B. A. Shook *et al.*, Myofibroblast proliferation and heterogeneity are supported by macrophages during skin repair. *Science* **362**, (2018).

58.   X. Zhou *et al.*, Circuit Design Features of a Stable Two-Cell System. *Cell* **172**, 744-757 e717 (2018).

59.   P. Roswall *et al.*, Microenvironmental control of breast cancer subtype elicited through paracrine platelet-derived growth factor-CC signaling. *Nat Med* **24**, 463-473 (2018).

60.   X. Li *et al.*, VEGF-independent angiogenic pathways induced by PDGF-C. *Oncotarget* **1**, 309-314 (2010).

61.   Y. Crawford *et al.*, PDGF-C mediates the angiogenic and tumorigenic properties of fibroblasts associated with tumors refractory to anti-VEGF treatment. *Cancer Cell* **15**, 21-34 (2009).

62.   H. F. Dvorak, Tumors: wounds that do not heal. Similarities between tumor stroma generation and wound healing. *N Engl J Med* **315**, 1650-1659 (1986).

63.   E. E. Dutton *et al.*, Peripheral lymph nodes contain migratory and resident innate lymphoid cell populations. *Sci Immunol* **4**, (2019).

64.   C. McQuin *et al.*, CellProfiler 3.0: Next-generation image processing for biology. *PLoS Biol* **16**, e2005970 (2018).

65.   J. W. Opzoomer *et al.*, ImmunoCluster provides a computational framework for the nonspecialist to profile high-dimensional cytometry data. *eLife* **10**, (2021).

66.   M. D. Wilkerson, D. N. Hayes, ConsensusClusterPlus: a class discovery tool with confidence assessments and item tracking. *Bioinformatics* **26**, 1572-1573 (2010).

67.   M. Nowicka *et al.*, CyTOF workflow: differential discovery in high-throughput high-dimensional cytometry datasets. *F1000Research* **6**, 748 (2017).

68.   A. Dobin *et al.*, STAR: ultrafast universal RNA-seq aligner. *Bioinformatics* **29**, 15-21 (2013).

69.   T. Stuart *et al.*, Comprehensive Integration of Single-Cell Data. *Cell* **177**, 1888-1902 e1821 (2019).

70.   L. Zappia, A. Oshlack, Clustering trees: a visualization for evaluating clusterings at multiple resolutions. *Gigascience* **7**, (2018).

71.   P. Angerer *et al.*, destiny: diffusion maps for large-scale single-cell data in R. *Bioinformatics* **32**, 1241-1243 (2016).

72.   Z. Gu, R. Eils, M. Schlesner, Complex heatmaps reveal patterns and correlations in multidimensional genomic data. *Bioinformatics* **32**, 2847-2849 (2016).

73.   A. M. Bolger, M. Lohse, B. Usadel, Trimmomatic: a flexible trimmer for Illumina sequence data. *Bioinformatics* **30**, 2114-2120 (2014).

74.   D. Kim, B. Langmead, S. L. Salzberg, HISAT: a fast spliced aligner with low memory requirements. *Nat Methods* **12**, 357-360 (2015).

75.   H. Li *et al.*, The Sequence Alignment/Map format and SAMtools. *Bioinformatics* **25**, 2078-2079 (2009).

76.   M. Lawrence *et al.*, Software for computing and annotating genomic ranges. *PLoS Comput Biol* **9**, e1003118 (2013).

77.   M. I. Love, W. Huber, S. Anders, Moderated estimation of fold change and dispersion for RNA-seq data with DESeq2. *Genome Biol* **15**, 550 (2014).

78.   M. Efremova, M. Vento-Tormo, S. A. Teichmann, R. Vento-Tormo, CellPhoneDB: inferring cell-cell communication from combined expression of multi-subunit ligand-receptor complexes. *Nat Protoc* **15**, 1484-1506 (2020).

79.   C. M. Elso *et al.*, Leishmaniasis host response loci (lmr1-3) modify disease severity through a Th1/Th2-independent pathway. *Genes Immun* **5**, 93-100 (2004).
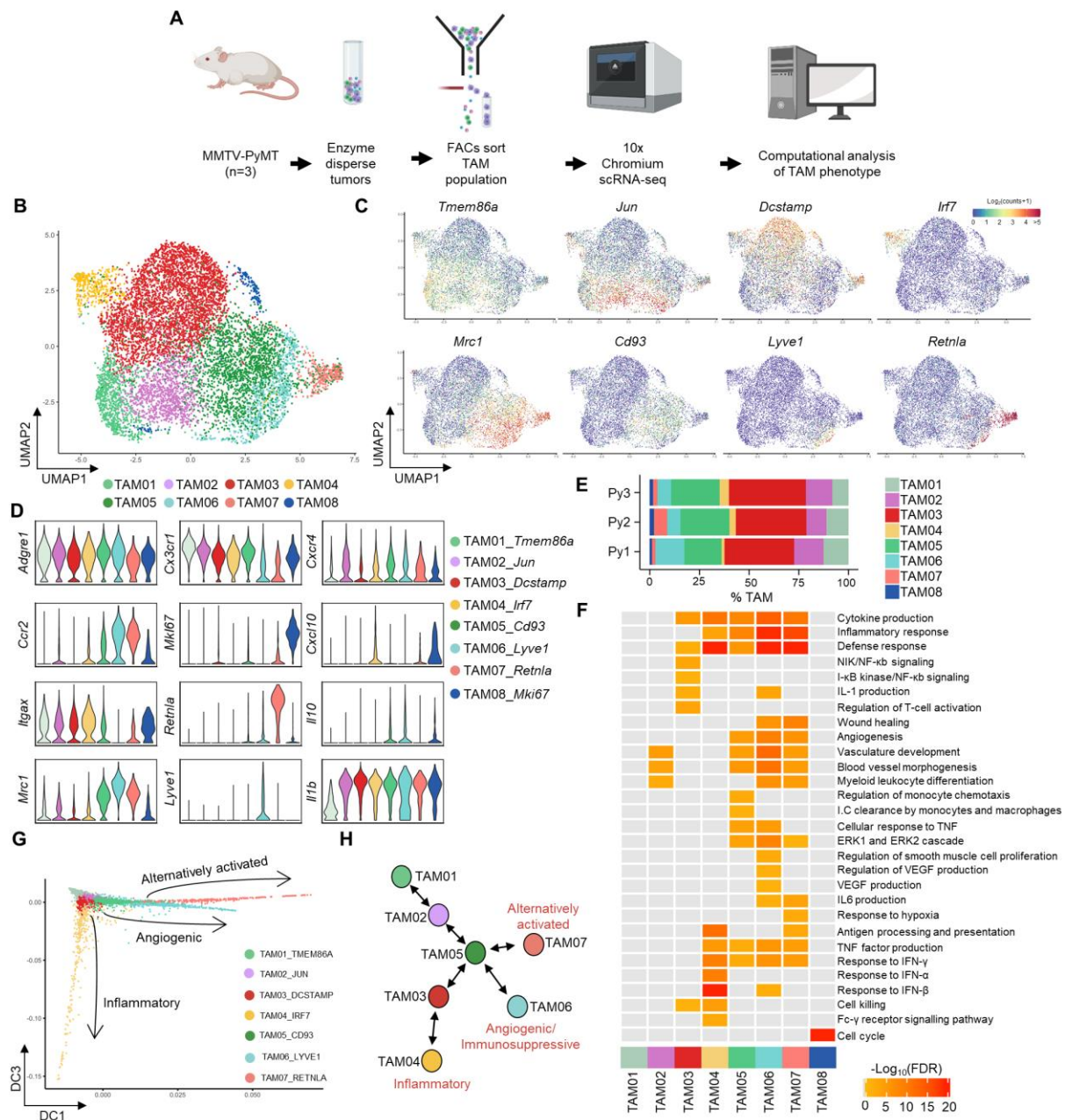
Figure 1. ScRNA-seq of TAMs in *MMTV-PyMT* tumors reveals three distinct polarization pathways. (**A**) Schematic outlining the scRNA-seq experimental workflow which was conducted for n=3 individual *MMTV-PYMT* tumors and mice, sequencing a total of 9,039 cells using the 10X Genomics' Chromium platform. (**B**) *UMAP* plot of sequenced TAMs colored by their associated cluster identity. (**C**) *UMAP* visualizations of predicted marker gene expression for distinct TAM clusters shown in (**B**). (**D**) Violin plots of selected genes associated with TAM cluster identity seen in (**B**). (**E**) The relative proportion of each TAM cluster across the individual *MMTV-PyMT* tumors analyzed. (**F**) Heatmap representing significantly upregulated GO pathway terms in one or more TAM clusters. (**G,H**) Scatter plot of single cells projected into two dimensions using diffusion maps, where each cell (dot) is colored by cluster identity, labeled with diffusion component (DC) space annotation representing lineage trajectories predicted by the *Slingshot* package (**G**) and schematic map of each TAM cluster's location along the respective trajectories (**H**).
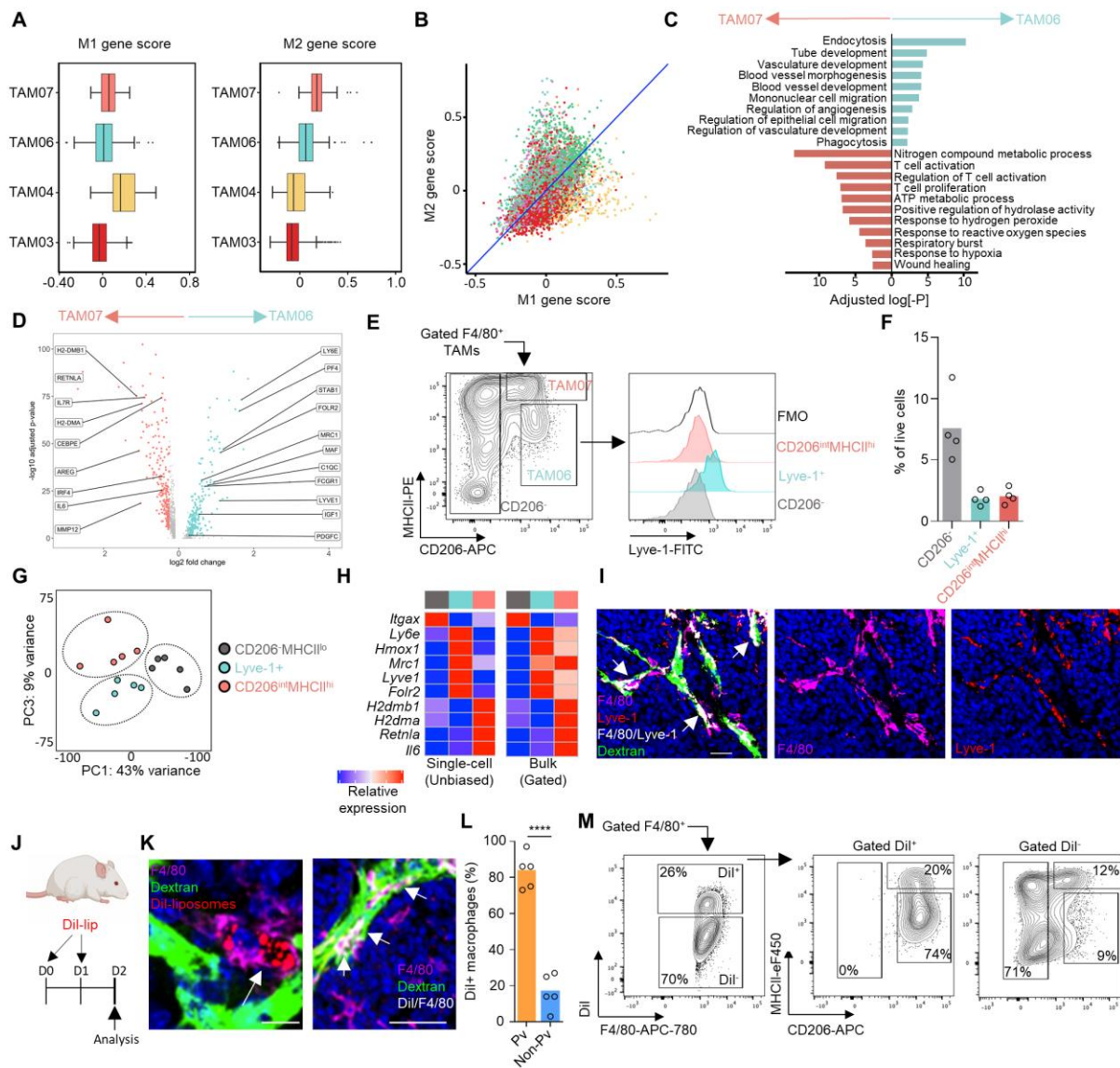
Figure 2. Lyve-1 marks a subset of TAMs which reside proximal to blood vasculature.
(**A-B**) Box and whisker plots (**A**) and scatter plot (**B**) showing normalized mean M1 and M2 associated gene scores across the indicated TAM clusters identified using scRNA-seq. (**C,D**) Subset unique, significantly upregulated GO terms (**C**) and individual genes (**D**) between the two subsets of pro-tumoral TAM. (**E**) FACs-gated live (7AAD⁻) F4/80ʰⁱ TAMs from enzyme-dispersed *MMTV-PyMT* tumors separated based on CD206 and MHCII expression (left panel) and assessed for Lyve-1 expression (right panel; colored shaded histograms) against that of the fluorescence minus one staining (FMO) control (open black line). (**F**) Quantification of the gated populations in (**E**) (n=4 tumors). (**G**) PCA plot of the bulk-sequenced TAM populations (n=5 tumors), using CD206⁻ and MHCII⁻ TAMs as a comparator. (**H**) Heatmaps comparing the relative expression of selected differentially expressed genes identified in the scRNAseq (left) and bulk RNA-seq (right panel), population color is indicative of the populations identified in (**G**). (**I**) Representative image of a frozen section of *MMTV-PyMT* tumor showing DAPI (nuclei; blue), i.v. dextran marking vasculature (green), F4/80 (magenta) and Lyve-1 (red), co-localizing pixels for Lyve-1 and F4/80 (white), scale bar 25µm. (**J-M**) Schematic for experimental approach to label pvTAMs using DiI-labeled liposomes (**J**). (**K**) Representative images of frozen sections of *MMTV-PyMT* tumors showing DAPI (nuclei; blue), i.v. dextran marking vasculature (green), DiI (red), F4/80 (magenta) and DiI/F4/80 co-localizing pixels are white (right panel alone), scale

bar 25μm (left panel) and 50μm (right panel). (**L**) Quantification of the spatial location of DiI$^+$ F4/80$^+$ TAMs (n=5 mice). (**M**) Analysis of the surface phenotype of DiI$^{+/-}$ TAM from enzyme-dispersed tumors within the F4/80$^+$ gate. Box and whisker plots; boxes show median and quartiles. Bar charts represent mean and the dots show individual tumors and mice. **** *P*<0.0001.
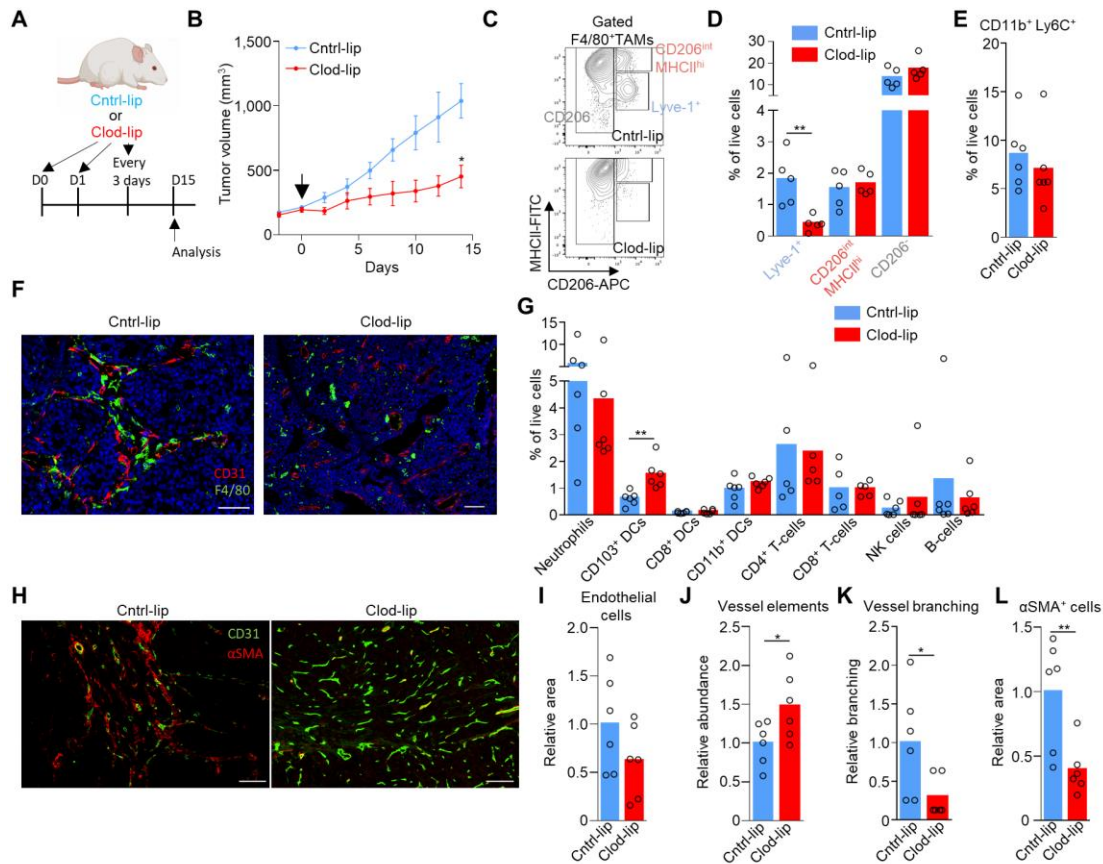
Figure 3. Lyve-1+ pvTAM depletion slows tumor growth and is associated with a concurrent loss of perivascular αSMA+ stromal cells. (**A**) Schematic for experimental approach and dosing strategy to deplete Lyve-1+ TAMs using clodronate-filled liposomes. Arrows represent days of treatment. (**B**) Growth curves of *MMTV-PyMT* tumors in mice treated with control PBS-filled liposomes (Cntrl-lip) or clodronate-filled liposomes (Clod-lip) as shown in panel (**A**), arrow marks the initiation of treatment, (cohorts of n=6 mice). (**C-L**) Tumors from (**B**) were excised at day 15 (post treatment initiation; n=5-6 tumors) and analyzed. (**C**) Representative contour plot gating of live (7AAD-) CD45+Ly6C-F4/80+CD206+ TAMs from enzyme-dispersed *MMTV-PyMT* tumors measured by flow cytometry and the abundance of the gates subsets (**D**). (**E**) Abundance of live (7AAD-) CD45+CD11b+Ly6C+ monocytes. (**F**) Representative image of a frozen section of *MMTV-PyMT* tumor from mice treated with cntrl- or clodronate-filled liposomes stained with DAPI (nuclei; blue) and antibodies against F4/80 (green) and CD31 (red). Scale bar represents 50μm (left panel) and 100μm (right panel). (**G**) The abundance of major immune cell types in the tumor microenvironment measured by flow cytometry. (**H-L**) Representative image of a frozen section of *MMTV-PyMT* tumor stained with antibodies against CD31 (green) and αSMA (red), scale bar represents 100μm (left and right panels) (**H**), and the quantification of relative CD31+ pixel area (**I**), number of distinct CD31+ endothelial vessel elements as assessed using immunofluorescence analysis stained frozen tissue sections (a total of n=12 sections, across n=6 mice per condition) (**J**), vessel branch points (**K**) and αSMA+ pixel area (**L**) A total of n=12 sections were analyzed across the 6 tumors in each cohort. Growth curve is presented as mean ± s.e.m and bar charts represent mean and the dots show individual data points from individual tumors and mice. * *P*<0.05, ** *P*<0.01, ***P*<0.001.
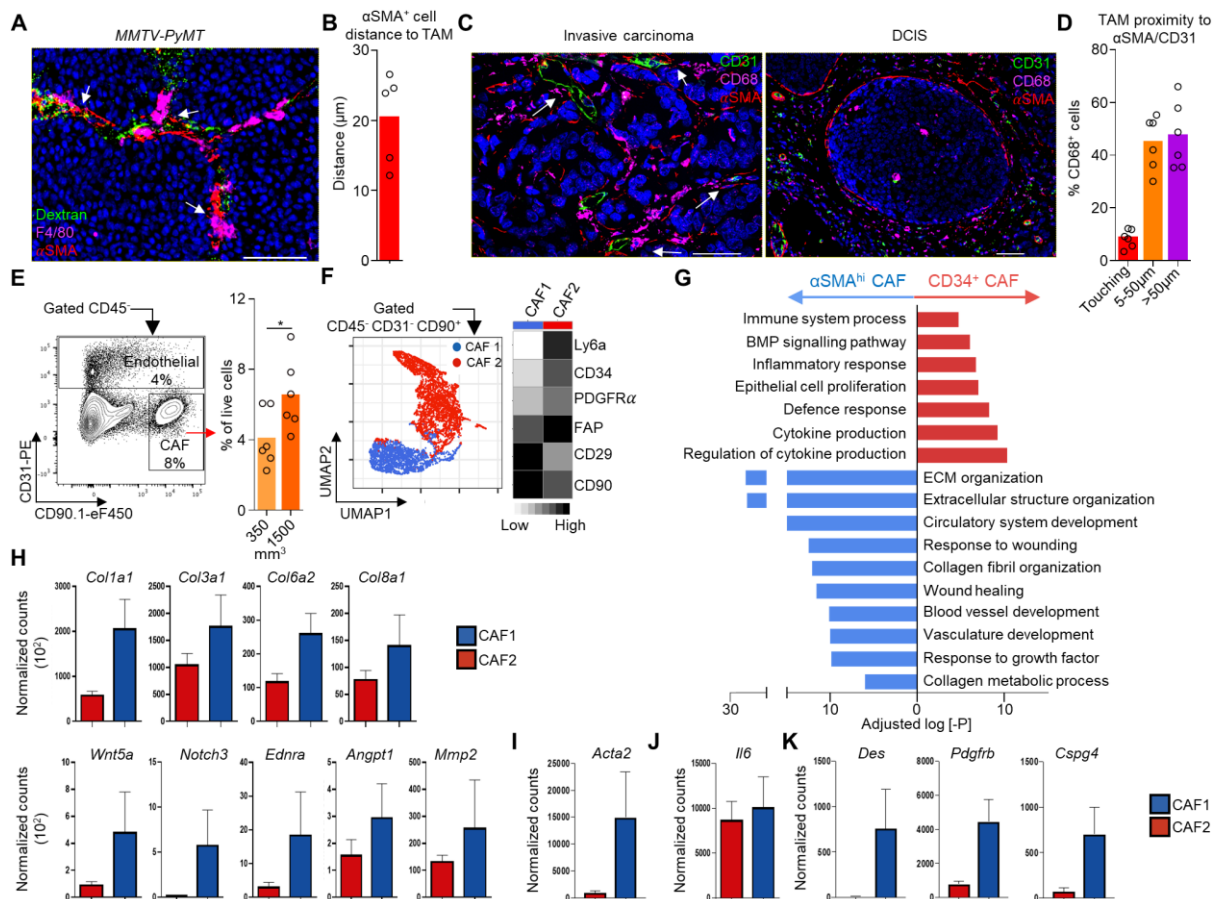
Figure 4. Lyve-1^{+} TAMs form a perivascular niche with pro-angiogenic pericyte-like αSMA[+] CAFs. (**A**) Representative image of a frozen section of *MMTV-PyMT* tumor stained with DAPI (nuclei; blue) and antibodies against F4/80 (magenta) and αSMA (red); functional vasculature was labeled *in vivo* using i.v. dextran-FITC (green). (**B**) Quantification of αSMA^{+} cells median distance from F4/80[+] TAM quantified from immunofluorescence images (n=5). (**C**) Representative image of a FFPE section from human invasive ductal mammary carcinoma (left) and DCIS (right) stained with DAPI (nuclei; blue) and antibodies against CD31 (green), CD68 (magenta) and αSMA (red), images representative of 4-6 patients. (**D**) Quantification of the spatial position of CD68^{+} TAM in proximity to SMA^{+} stroma touching CD31^{+} vessels (<50μm is regarded perivascular) across multiple ROIs (n=5 tumors). (**E**) Representative flow cytometry gating strategy for live (7AAD^{-}) CD45^{-} cells and CD31^{+} endothelial cells and CD90^{+} CAFs (left) and the abundance of CAFs at different tumor volumes (right), n=6 mice per condition. (**F**) Identification of CAF subsets by unsupervised clustering from multiparametric flow cytometry data using the markers shown in the heatmap (right). *UMAP* plot shows individual cells colored by their unsupervised clustering assignment (left), n=4 mice. (**G-K**) Bulk RNA-sequenced CAF subsets from *MMTV-PyMT* tumors (n=5 mice) transcriptomes were investigated. GO pathway analysis and plot shows the selected GO terms based on differentially expressed genes of the two CAF subsets (**G**), and bar plots depicting normalized gene expression values for the indicated genes associated with angiogenesis (**H**), *Acta2* (**I**) and *Il6* (**J**) and pericyte-associated markers (**K**). Differences in gene expression in panels **H**, **I** and **K** are all *P*<0.0001. Bar charts represent mean, error bars represent s.d. and the dots show individual data points from individual tumors and mice. Scale bars represent 50μm.
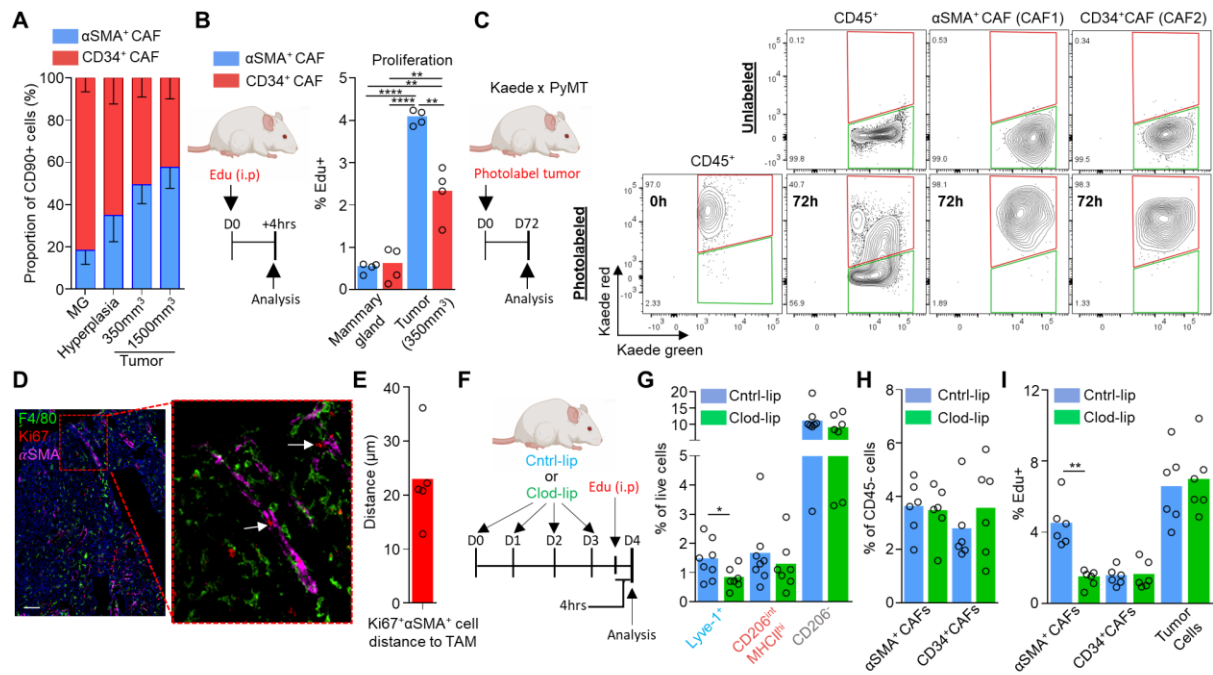
Figure 5. Lyve-1⁺ TAMs orchestrate αSMA⁺ CAF expansion within the perivascular niche of the tumor. (**A**) Abundance of the respective CAF populations during distinct stages of tumor progression, n=6 mice per stage. (MG; mammary gland). (**B**) Schematic for experimental approach and dosing Edu into *MMTV-PyMT* mice to assess *in vivo* proliferation (left), proportion EdU⁺ cells within each CAF subset (right). (**C**) Established tumors in *Kaede MMTV-PyMT* mice were photoconverted to kaede red and then at 72h post photoconversion tumors were analyzed (schematic left) for their respective kaede red/green proportion using flow cytometry for evidence of peripheral recruitment (kaede green cells). A representative unconverted tumor is shown for comparison (right top). (**D-E**) Representative image of a frozen section of *MMTV-PyMT* tumor stained with antibodies against F4/80 (green), αSMA (magenta) and the proliferation marker Ki67 (red). White arrows show αSMA⁺Ki67⁺ cells in contact with F4/80⁺ TAMs (**D**) and quantification of Ki67⁺ αSMA⁺ cells median distance from F4/80⁺ TAMs quantified from immunofluorescence images across multiple tumors (n=5) (**E**). (**F-I**) Schematic for experimental approach and dosing strategy to acutely deplete Lyve-1⁺ pvTAM with clodronate-filled liposome treatment for 4 days (**F**). (**G**) Abundance of TAM populations following cntrl- or clodronate-filled liposome treatment (n=6 mice cntrl-lip and n=5 mice clod-lip). (**H**) Abundance of CD45⁻ cell populations (cohorts of n=6 mice) post 4 days treatment with either cntrl or clodronate-filled liposomes. (**I**) Proportion of EdU⁺ cells within each CD45⁻ cell subset, (cohorts of n=6 mice). Bar charts represent mean, error bars represent s.d. and the dots show individual data points from individual tumors and mice. *$P<0.05$, ** $P<0.01$, ***$P<0.001$, ****$P<0.0001$.
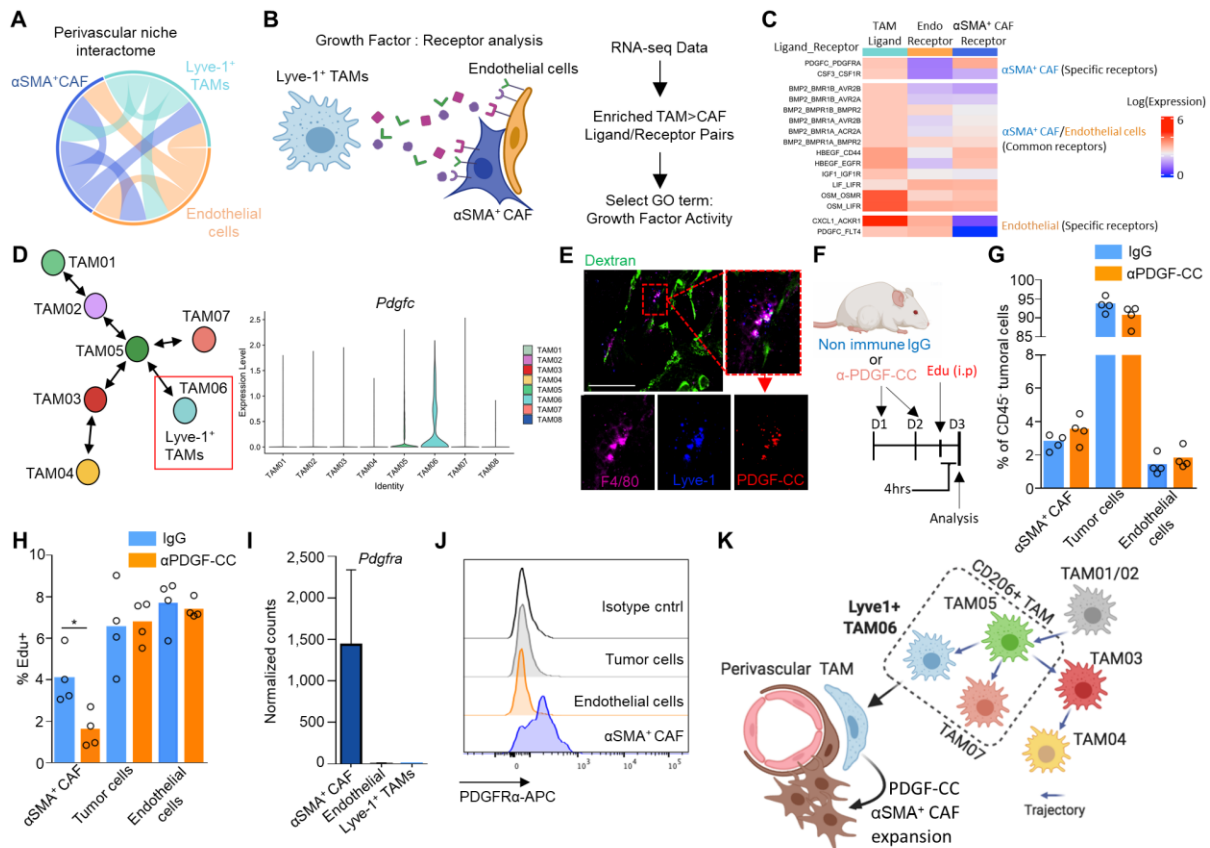
Figure 6. Lyve-1⁺ TAMs communicate to αSMA⁺ CAFs in the perivascular niche via a pro-proliferative PDGF-CC:PDGFR-α interaction (**A**) Circos plot showing predicted crosstalk of perivascular ligand-receptor interactions as identified by *CellPhoneDB* from the respective RNA-seq datasets. Outer sectors and links between sectors are weighted according to the total number of annotated ligand-receptor interactions between each respective cell type. (**B**) Schematic representing the method of cell type ligand-receptor interactome generation. (**C**) Heatmap showing the Lyve-1⁺ TAM and αSMA⁺ CAF population-specific secretome generated using data from (**A**) and the method outlined in (**B**) diagram displaying the ligand:receptor pairs between Lyve-1⁺ TAMs and αSMA⁺ CAFs and endothelial cells. The analysis highlighted a unique PDGF-CC:PDGFRα interaction specific to Lyve-1⁺ TAMs and αSMA⁺ CAFs. (**D**) Schematic map of each TAM cluster's location along the respective trajectories marking the Lyve-1⁺ TAM population (left) and violin plots of *Pdgfc* expression associated with TAM clusters (right). (**E**) Representative image of a frozen section of *MMTV-PyMT* tumor stained with antibodies against F4/80 (magenta), Lyve-1 (blue), PDGF-CC (red), the vessels are marked by dextran (green). (**F-H**) Schematic for experimental approach and dosing strategy to acutely inhibit PDGF-CC signalling using an anti-PDGF-CC neutralizing antibody (**F**). Abundance of indicated cell populations (**G**). Proportion of EdU⁺ cells within each CD45⁻ cell subset, (cohorts of n=4 mice) (**H**). (**I**) Bar plot depicting normalized gene expression values for *Pdgfra* in the bulk RNA-sequenced populations (left) across n=5 mice. (**J**) Representative histograms of surface PDGFRα staining on the indicated cells against isotype antibody staining of gated using flow cytometry analysis from enzyme-dispersed *MMTV-PyMT* tumors. (**K**) Schematic overview of the perivascular niche. Images in panel (B and J) was created using *BioRender* software. Bar charts represent mean and the dots show individual data points from individual tumors and mice, error bars represent s.d. * *P*<0.05.

Auxiliary Supplementary Tables

Table S1. List of up regulated genes for scRNA-seq TAM clusters versus all other clusters.

Table S2. List of up regulated genes for scRNA-seq TAM clusters TAM06 versus TAM07.

Table S3. List of up regulated genes for facs-sorted bulk RNA-seq of CD45$^-$ stromal populations versus all other CD45$^-$ stromal populations.

Table S4. List of CellPhoneDB ligand-receptor interactions between perivascular niche cell populations with mean values for ligand-receptor interactions.

Table S5. List of putative growth factor ligand-receptor interactions derived from CellPhoneDB data with relative gene expression.
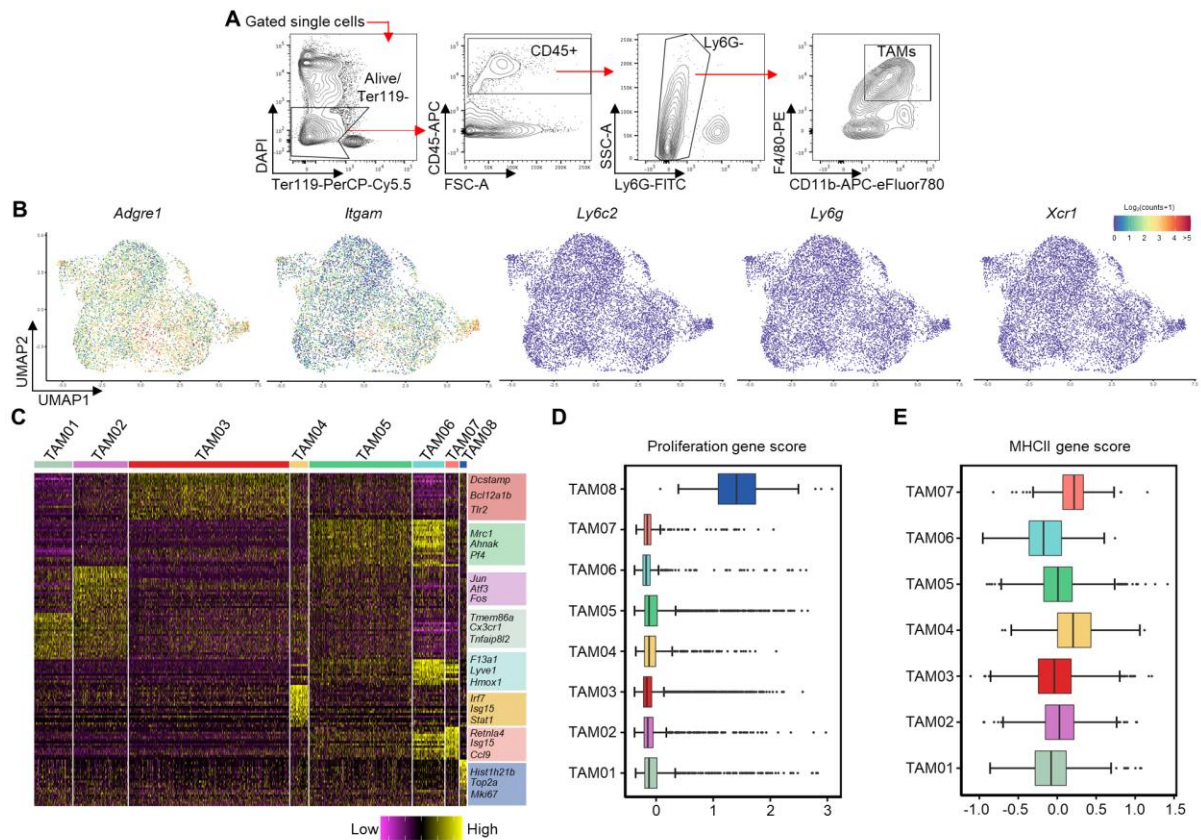
Supplementary Figures

Figure S1. scRNA-seq of TAMs identifies distinct polarization states within the tumor microenvironment. (**A**) Representative gating strategy for live (7AAD⁻) TAMs for sorting using the indicated surface markers from enzyme-dispersed *MMTV-PYMT* tumors used in scRNA-seq sample preparation analyzed in Fig. 1 and 2. (**B**) UMAP plots of the 9,039 TAMs sequenced using the 10X Genomics' Chromium platform across n=3 tumors displaying the expression of marker genes used to isolate TAM single cells in (**A**). (**C**) Heatmap showing top differentially expressed genes within each TAM cluster shown in Fig.1b, selected genes for each cluster are highlighted to the right of the heatmap. (**D,E**) Gene scores across all TAM clusters for proliferation (**D**) and MHCII associated genes (**E**). Box and whisker plots, the boxes show median and upper and lower quartiles and whiskers shows the largest value no more than 1.5*IQR of the respective upper and lower hinges, outliers beyond the end of the whisker are plotted as individual dots.
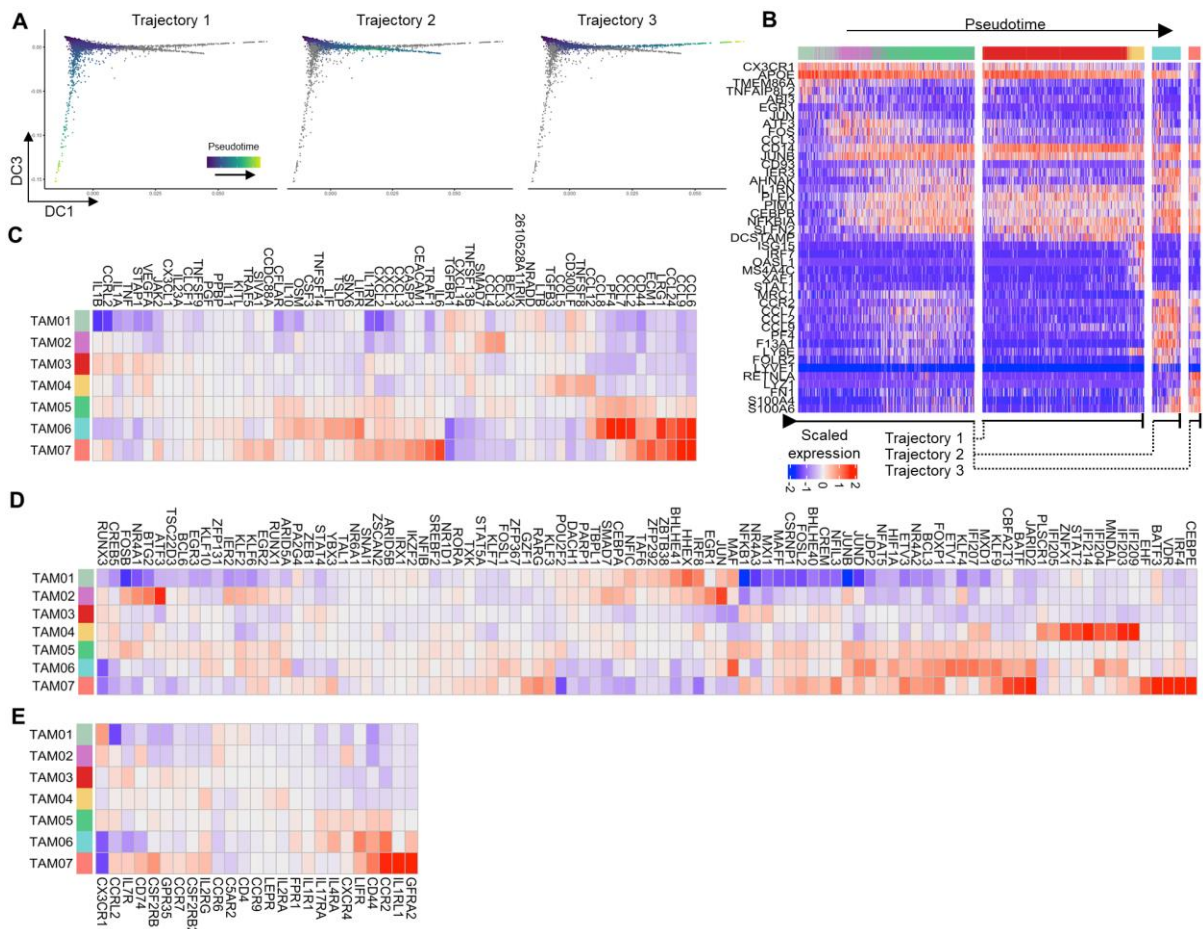
Figure S2. Trajectory analysis of scRNA-seq of TAMs reveals polarization-specific transcription factors and cytokine signatures associated with transcriptomic state. (**A**) Diffusion component (DC) plot showing single cells colored by pseudotime value for each distinct trajectory predicted by *Slingshot* trajectory analysis. Cells that are not associated with a given trajectory are greyed out. (**B**) Heatmap of selected genes varying significantly across trajectory. Single cells (columns) are arranged left to right by pseudotime value within their labeled trajectories, branching points are indicated beneath the heatmap. (**C**-**E**) Heatmaps representing chemokine, cytokine and complement factor genes (**C**), transcription factor genes (**D**) and additional chemokine, cytokine and complement receptor genes (**E**) that vary significantly across the predicted *Slingshot* trajectories.
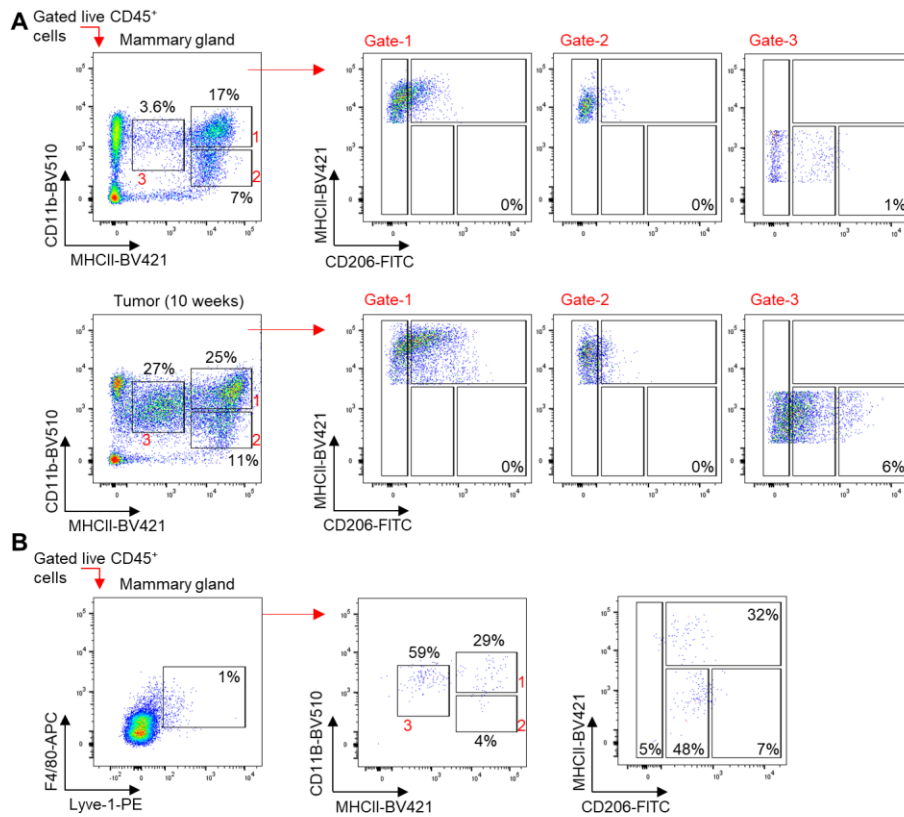
Figure S3. Comparison of macrophage phenotypes in the mammary gland and *MMTV-PyMT* tumors. Representative flow cytometry gating strategy of live (7AAD^{-}) CD45^{+} cells assessed according to Franklin et al (35) to resolve macrophage subsets and comparison to those used in the current study. (**A**) Flow cytometry dot plots of enzyme-dispersed tissue from either non-malignant mammary gland (from age-matched PyMT[-] mice) or *MMTV-PyMT* tumors from 10 week-old mice were stained with antibodies against the indicated markers. Percentage indicated represents the proportion of events falling into the MHCII^{lo} CD206^{hi} gate (where Lyve-1^{+} pvTAMs are identified). (**B**) Dot plots from flow cytometry analysis of enzyme-dispersed tissue from non-malignant mammary gland gating for live (7AAD^{-}) CD45^{+} tissue resident Lyve-1^{+} macrophages (left panel) and their distribution for the markers used in (**A**).
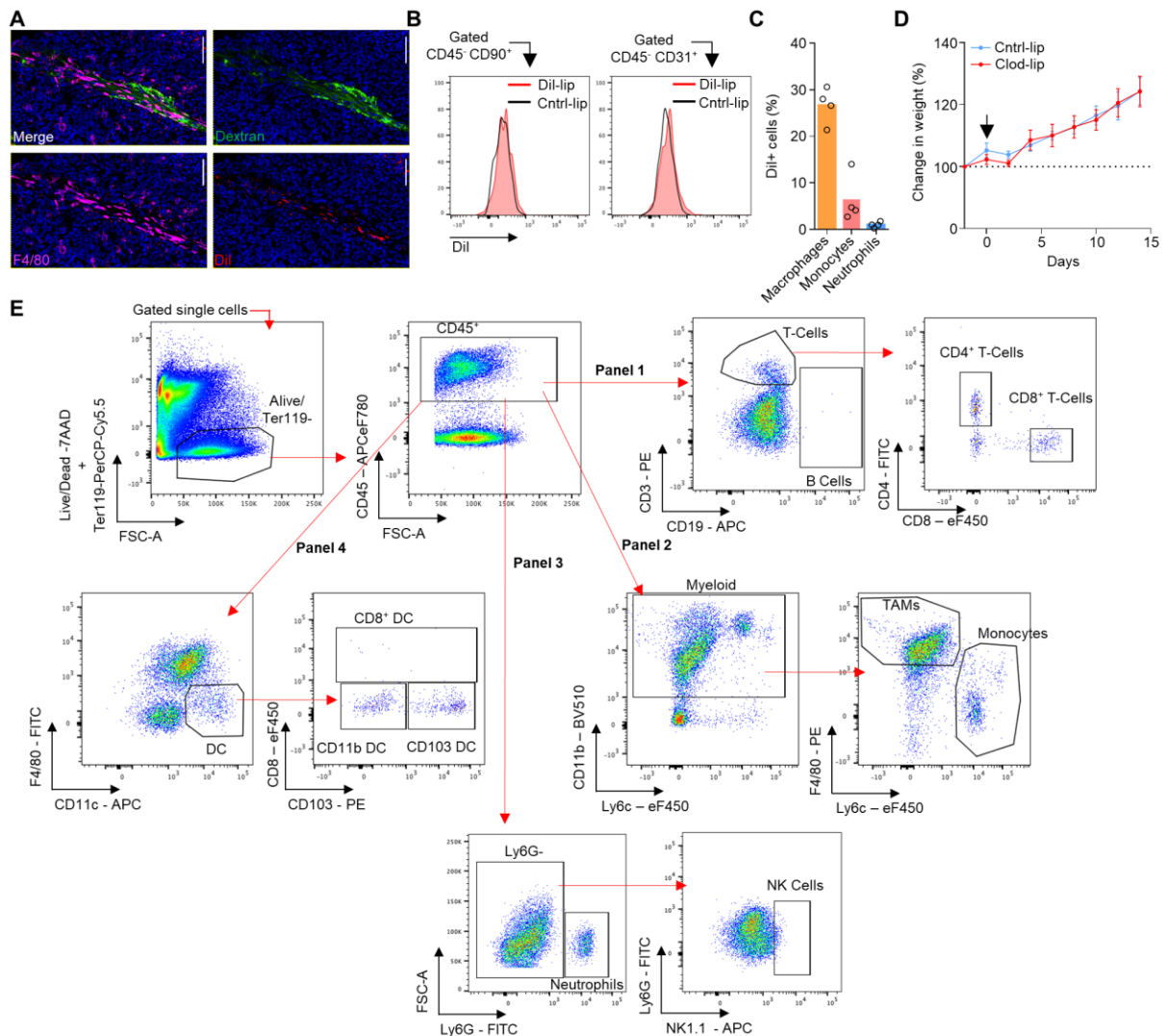
Figure S4. Liposomes are specifically taken up by a PvTAM subset. (A) Representative image of a frozen section of *MMTV-PyMT* tumor showing DAPI (nuclei; blue), i.v. dextran marking vasculature (green), Dil from the liposomes (red) and antibody staining against F4/80 (magenta), scale bar represents 50µm. (**B**) Representative histograms showing Dil-containing liposome uptake (red filled histogram) against PBS-filled liposome treated mice (open black line histogram) in CD90$^+$ CAF and CD31$^+$ endothelial cells in the CD45$^-$ gate of enzyme-dispersed tumors from *MMTV-PyMT* mice treated as shown in Fig. 2J and assessed using flow cytometry, representative of n=3 mice**. (C**) Proportion of live (7AAD$^-$) gated tumor-resident phagocytic populations with detectable Dil uptake as assessed using flow cytometry (n=4 mice). (**D-E**) Tumor bearing *MMTV-PyMT* mice treated with control PBS-filled liposomes (Cntrl-lip) or clodronate-filled liposomes (Clod-lip) using the treatment regimen shown in Fig. 3A, showing the percentage change in mouse weight over the course of the experiment (**D**), representative gating strategy for identifying different tumour-resident leukocyte populations in enzyme-dispersed tumors taken at day 15 post initiation of treatment with the respective liposomes (**E**). Bar charts represent mean and the dots show individual data points from individual tumors and mice. * *P*<0.05, ** *P*<0.01.
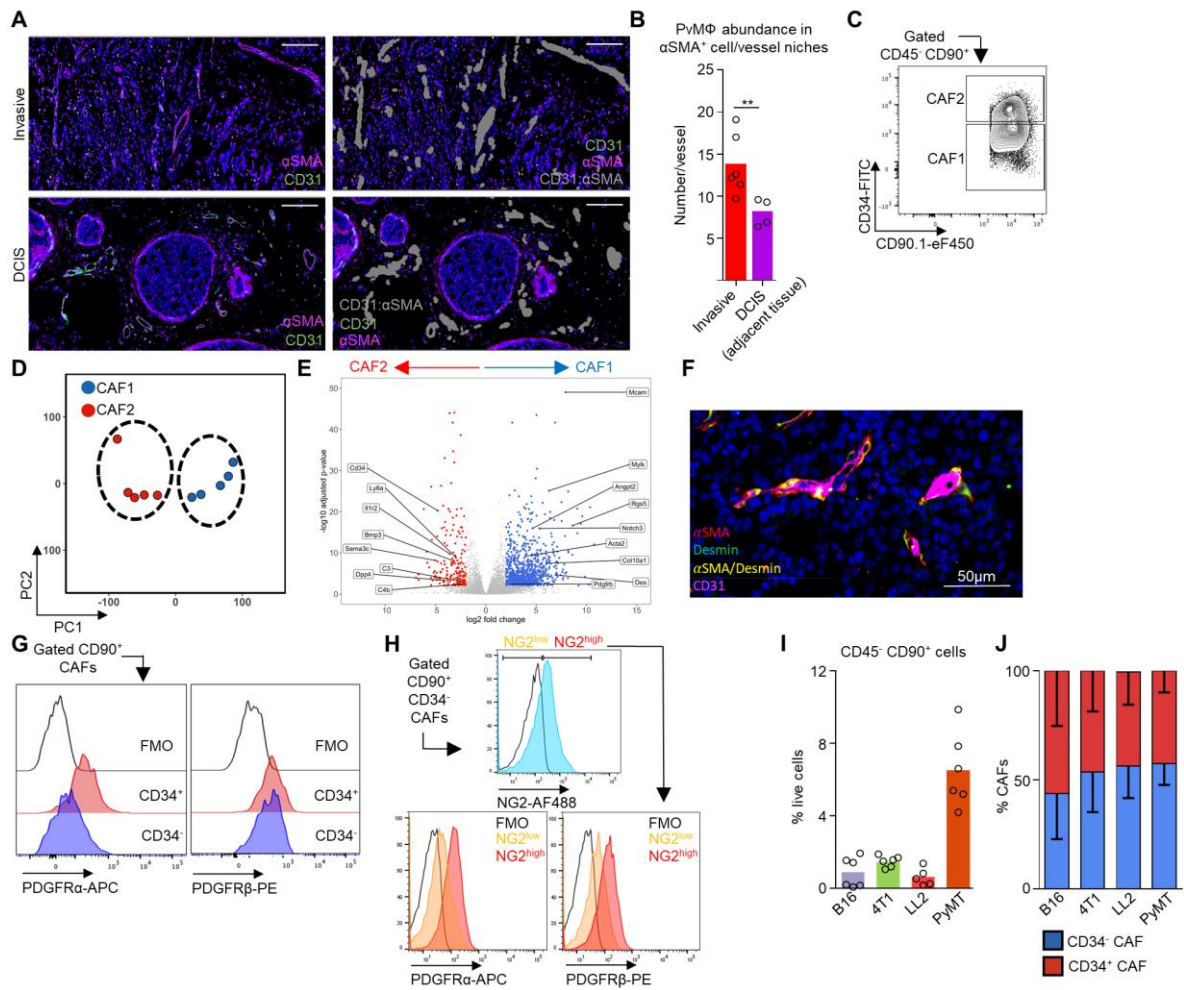
Figure S5. The perivascular niche and mesenchymal cell heterogeneity in murine models of cancer. (**A**) Representative image of a FFPE section from human invasive ductal mammary carcinoma (top) and DCIS (bottom) stained with DAPI (nuclei; blue) and antibodies against CD31 (green) and αSMA (magenta) where these cells were touching (perivascular niche) cells were labeled grey, CD68 staining events are also displayed on the image, where events less or more than 50 µm from a vessel labeled orange and yellow respectively. Scale bar indicates 150 µm. (**B**) Quantification of the number of CD68+ TAMs within the perivascular niche of SMA+ stroma touching CD31+ vessels (<50µm is regarded perivascular) identified from (**A**), assessed across multiple ROIs (n=6 invasive tumors and n=4 DCIS). (**C**) Representative gating strategy for flow cytometry sorting the predicted subsets of CAFs by unsupervised clustering analysis. (**D-E**) Bulk RNA-seq of the CD34+/- CAF subsets, showing PCA plot of the bulk-sequenced CAF populations showing the difference in CAF transcriptome (**D**), differentially expressed genes between CD34+/- CAF populations (**E**) across n=5 tumors and mice. (**F**) Representative confocal image of a frozen *MMTV-PyMT* tumor section showing DAPI (nuclei; blue), and antibody staining against CD31 (magenta), αSMA (red), desmin (green) and αSMA/desmin co-localization (yellow). Representative of multiple sections from n=4 tumors and mice. Scale bar represents 100µm. (**G-H**) Representative histogram of live (7AAD-) CD90+CAFs gated using flow cytometry in a representative enzyme-dispersed *MMTV-PyMT* tumor; histogram shows surface staining for the PDGFRα and PDGFRβ on CD34+/- CAFs (shaded histograms) against that of the fluorescence minus one (FMO) control (open histogram) (**G**), or gated live (7AAD-) CD90+CD34- CAFs showing surface staining for NG2 (top; shaded histogram) and the respective expression of PDGFRα and PDGFRβ on the CD34- CAFs sub-gated for either 'high' or 'low' surface NG2 expression (bottom; shaded histograms) against that of the FMO control (all; open histograms) (**H**). (**I-J**) Mice were injected with the indicated tumor cells and

when tumors reached 1500mm^3 they were enzyme-dispersed and analyzed by flow cytometry for the abundance of live (7AAD$^-$) CD45$^-$CD31$^-$CD90$^+$ CAFs (**I**) and the relative proportions of CD34$^+$ and CD34$^-$ CAFs (**J**) across n= 5-6 mice per model. Bar charts represent mean and error bars s.d., dots show individual data points from individual tumors and mice.
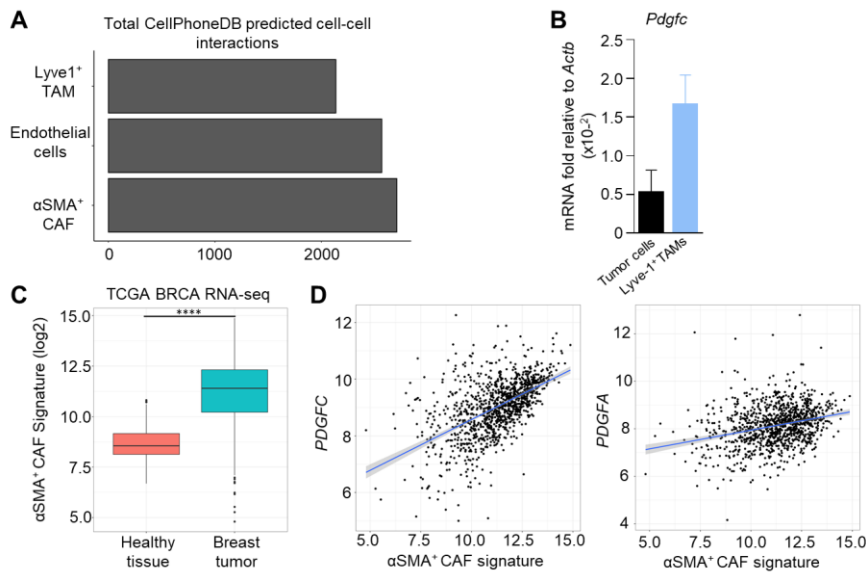

Figure S6. A αSMA$^+$ CAF signature correlates with *PDGFC* expression in human breast cancer (**A**) The number of total potential ligand and receptor interactions identified per bulk RNA-sequenced cell type that participate in paracrine and autocrine signaling networks in the perivascular niche. (**B**) *Pdgfc* mRNA expression relative to the housekeeping gene *Actb* in FACS-sorted tumor cells (CD45$^-$CD31$^-$CD90$^-$; n=6) and Lyve-1$^+$ TAMs (n=3). (**C**) Normalized log2 RNA-seq counts for the TCGA-BRCA dataset for the αSMA^{hi} CAF gene signature in non-malignant breast tissue (n=112) and primary breast carcinoma tissue (n=1,093). (**D**) Scatterplot of αSMA$^+$ CAF gene signature score (x axis) and *PDGFC* (y axis) (Pearson's r = 0.547, p < 0.0001) (left) or *PDGFA* (y-axis) (Pearson's r = 0.286 p < 0.0001) (right) from the TCGA-BRCA RNA-seq dataset, n=1,093. Box and whisker plots, the boxes show median and upper and lower quartiles and whiskers shows the largest value no more than 1.5*IQR of the respective upper and lower hinges, outliers beyond the end of the whisker are plotted as individual dots. Bar charts represent mean, error bars represent s.e.m. **** *P*<0.0001.